

The Structure and Dynamics of Ringed Galaxies. V. The
Kinematics of NGC 1512, NGC 3351, NGC 4725, and NGC
4736

R. Buta – Australian National University

Deposited 08/05/2019

Citation of published version:

Buta, R. (1988): The Structure and Dynamics of Ringed Galaxies. V. The Kinematics of NGC 1512, NGC 3351, NGC 4725, and NGC 4736. *Astrophysical Journal Supplement Series*, vol. 66(p. 233). DOI: <https://doi.org/10.1086/191255>

THE STRUCTURE AND DYNAMICS OF RINGED GALAXIES. V. THE KINEMATICS OF NGC 1512, NGC 3351, NGC 4725, AND NGC 4736

R. BUTA¹

Department of Astronomy and McDonald Observatory, University of Texas at Austin

Received 1987 April 13; accepted 1987 September 16

ABSTRACT

The spirals NGC 1512, NGC 3351, NGC 4725, and NGC 4736 are four large nearby examples of ringed galaxies whose kinematic properties are studied in this paper by means of H α Fabry-Perot interferometry. Velocity fields are first analyzed in terms of pure circular motions, and approximate rotation curves and masses are derived. Then the kinematics of the inner rings alone are studied using a velocity–position angle diagram, and analyzed in terms of circular rotation, rotation plus uniform expansion or contraction, an unperturbed dispersion orbit, or a perturbed oval bar orbit. The results show first that the inner ring in each of these galaxies is a region where H α emission is enhanced compared with regions inside or outside the ring, and hence that the ring is a zone of active star formation. The pure circular rotation analyses show that in general the kinematic line of nodes does not agree with the position angle of the major axis of the inner ring, suggesting either that the latter is intrinsically oval in shape on average or that expanding/contracting motions are prevalent in rings. Only for NGC 4725 does the velocity–position angle diagram of the inner ring show an unmistakable asymmetry indicative of significant noncircular motions. A possible interpretation is that this ring is expanding at $52 \pm 7 \text{ km s}^{-1}$ and rotating at $219 \pm 4 \text{ km s}^{-1}$. However, for all four galaxies models of stable elliptical orbits provide fits to the inner rings which are just as acceptable as pure rotation or expanding/contracting ring fits. In no case is a unique kinematic model of the ring achievable, owing to inadequate knowledge of the parent galaxy orientation parameters.

Subject headings: galaxies: individual (NGC 1512, NGC 3351, NGC 4725, NGC 4736) —
 galaxies: internal motions — galaxies: structure — interferometry —
 nebulae: H II regions

I. INTRODUCTION

Ringed galaxies are interesting for several reasons. First, they form a distinctive morphological subgroup spanning almost the entire disk galaxy sequence, including lenticulars (de Vaucouleurs 1959; Sandage 1961), and hence serve to provide a focus for understanding galaxy morphology (Kormendy 1979, 1982). Since ringlike or pseudo-ring-like patterns are evident in up to 50% of disk galaxies of early to intermediate Hubble type (e.g., de Vaucouleurs 1963), it is clear that the ring phenomenon is an important aspect of galaxy structure. Second, on the basis of recent dynamical models (Schwarz 1979), the ringlike patterns are believed to be linked to the principal orbit resonances which arise in a galaxy whose internal dynamics is influenced by a nonaxisymmetric perturbation, such as a bar or a density wave. This gives rings the potential of being useful probes of galaxy dynamics and structure, and is the main inspiration of this series of papers.

In Buta (1986*a*, *b*, 1987*a*, *b*, hereafter Papers I–IV), I have attempted to present a useful, but by no means complete, picture of the properties of ringed galaxies using two approaches. The first, or statistical approach, involved the measurement of the distributions of apparent shapes, relative sizes, and apparent orientations of rings to determine their true shapes and orientations with respect to bars in the planes of galaxies. The second, or individual approach, involved the measurement of the photometric and kinematic properties of several selected examples in order to provide a more appropriate data base for the focus of dynamical models. The two approaches together have, on the one hand, provided a strong case for a link between rings in normal galaxies and orbital resonances with a bar, and, on the other hand, they have illustrated the great diversity in properties within the class. The most important properties which make the rings themselves interesting are their preference for noncircular shapes, their tendency to be intrinsically aligned either parallel or perpendicular to bars, the existence of preferred ratios in double-ring systems, and the tendency for rings in spirals to be zones of heightened star formation activity compared with surrounding regions. It is clear that in order to establish these properties better and to understand further the nature of rings, it is necessary to examine as many individual cases as

¹Visiting Astronomer, Cerro Tololo Inter-American Observatory, which is operated by the Association of Universities for Research in Astronomy, Inc., under contract with the National Science Foundation; and Anglo-Australian Observatory.

possible. It is the purpose of this paper to explore the kinematic properties of four more excellent ringed systems.

The galaxies to be studied here are well-known, nearby spirals. Three are barred: NGC 1512, NGC 3351, and NGC 4725. The fourth, NGC 4736, has been the subject of many previous photometric and kinematic studies. Together these four objects will give us a useful picture of the variety in ring kinematics, and will provide further support for the properties derived for the other galaxies studied in Papers I–IV.

Section III describes the new velocity observations. Velocity fields are presented in § IV based on these observations and any available published data. The data are then analyzed in §§ V and VI. Conclusions are presented in § VII.

II. BASIC PARAMETERS

Table 1 summarizes a number of the basic parameters of the four sample galaxies published in various catalogs. Photometric parameters are taken from preliminary lists intended for the Third Reference Catalogue of Bright Galaxies (currently under production at the University of Texas), and are needed for establishing distances to the galaxies. One galaxy for which new multiaperture photoelectric photometry was obtained is NGC 1512; the photometry is based on observations with the Cerro Tololo Inter-American Observatory 0.91 m telescope (Table 2). The distance moduli given in Table 1 are based on averages of several methods, including the luminosity index (de Vaucouleurs 1979) and the Tully-Fisher relation (Bottinelli *et al.* 1983; Aaronson *et al.* 1982), and are not very accurate. Summaries of distances from individual methods and their errors are given by Buta (1984).

Other parameters such as the photometric major axis and inclination are taken from published surface photometry where available, the *Second Reference Catalogue of Bright Galaxies* (de Vaucouleurs, de Vaucouleurs, and Corwin 1976, hereafter RC2) or other sources. Especially well studied photometrically are NGC 4725 (Borson 1981; Wevers 1984; Kent 1984) and NGC 4736 (Borson 1981; Kent 1987; S. M. Kent 1987, private communication). References for the various parameters are given in Table 1.

III. VELOCITY OBSERVATIONS

The new velocity measurements are based on observations with the McDonald Observatory Mark II Fabry-Perot interferometer and the TAURUS Fabry-Perot interferometer of the Anglo-Australian Observatory. In addition to these measurements, a small number of individual H II regions in NGC 4725 were observed with the McDonald Observatory Image-Dissector Scanner (IDS). Useful discussions of the reduction and analysis of Fabry-Perot data are given by Tully (1974), Pence (1978), and de Vaucouleurs and Pence (1980).

The Mark II interferometer is the second of two Fabry-Perot systems which have been in use at McDonald Observatory. The Mark I system has been described in detail by de Vaucouleurs and Pence (1980). The two instruments differ mainly in scale at the image plane and in the size of the detector. The basic system consists of a collimator-etalon-camera combination. The image tube used for the present

work is a 40 mm VARO two-stage fiber optics tube selected for optimum sensitivity and resolution over a large fraction of the field and for minimum dark emission. A tilted 60 mm etalon (FP2, by Optical Surfaces, Ltd.) having a free spectral range of 281.9 km s^{-1} at H α was used for all of the observations. Isolation of the H α line in different galaxies was accomplished with a library of 2 inch (5 cm) diameter interference filters having a half-maximum width of 10 Å, and separated by 5 or 10 Å.

Table 3A summarizes the details on the 17 interferograms of NGC 3351, NGC 4725, and NGC 4736 that were analyzed for this work. All were obtained by G. and A. de Vaucouleurs in 1981 March and April at the f/13.6 Cassegrain focus of the McDonald Observatory 2.1 m telescope. In addition, interference filter photographs centered near the redshifted H α wavelength and in a nearby continuum wavelength were obtained with the same instrument with the etalon removed (see Table 3B). These are illustrated in Figure 1 (Plate 1), while two interferograms of each galaxy in orthogonal position angles are shown in Figure 2 (Plate 2). Except for NGC 4736, the fringes produced by the etalon are not necessarily continuous but are broken up, owing to modulation of the pattern by individual H II regions. This is unlike the situation encountered in some late-type spiral and irregular galaxies (e.g., NGC 4449), where the H II regions are embedded in a disk of diffuse emission that produces considerably more continuous, better defined fringes than do discrete H II regions (see, for example, de Vaucouleurs and Pence 1980). It is well known that individual H II regions can distort the fringes and yield larger velocity errors (an excellent discussion of this problem is given by Tully 1974). Such errors can be minimized by combining several interferograms taken with different centers and in various position angles, and then averaging the data in finite cells containing many velocity points.

The interferograms were scanned with the PDS microdensitometer of the University of Texas. Reductions were carried out according to the procedures described by de Vaucouleurs and Pence (1980), with programs written by Pence (1978). The reader is referred to a discussion by Buta (1984) for details. After correction for significant pincushion distortion, the linear scale of the interferograms was measured to be $22''.98 \pm 0''.02 \text{ mm}^{-1}$ based on precisely known star positions in two fields.

Estimates of the velocity errors were made by dividing each galaxy field into $10'' \times 10''$ square pixels, and then comparing velocity measurements within each cell either between different interferograms or between independent observers. Published data are available for NGC 3351 (Peterson *et al.* 1976, hereafter PRFT) and for NGC 4736 (van der Kruit 1976*a*). The results indicate that the Mark II data are best for NGC 4736, which is not surprising, since the fringes in this case are very well defined (see Fig. 2). Internal errors appear to be on the order of 10 km s^{-1} per velocity point, while the comparison with van der Kruit (1976*a*) indicates external errors of about 13 km s^{-1} per velocity point. Both of these are probably slight overestimates, since a $10'' \times 10''$ cell in this case will be affected somewhat by the rotation across the cell. For the fainter fringes in NGC 3351 and NGC 4725, internal

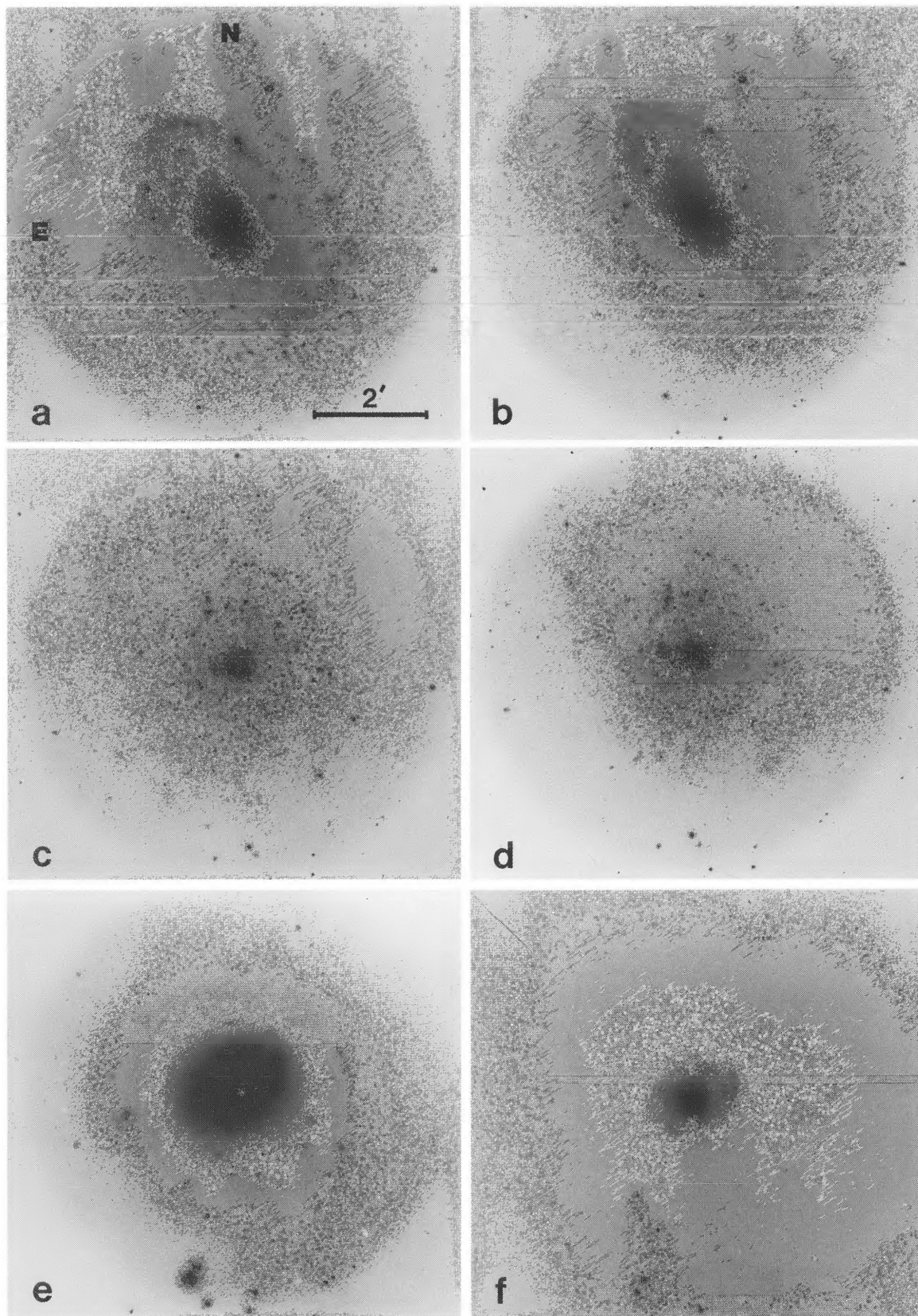


FIG. 1.—Interference filter photographs taken with the McDonald Observatory Mark II interferometer. Top panels show NGC 4725, middle panels show NGC 3351, and bottom panels show NGC 4736. The left-hand panels are taken in a narrow-band filter which transmits the redshifted $H\alpha$ wavelength, while the right-hand panels are taken in a neighboring wavelength in the continuum. Refer to Table 3B for other details of these photographs. In (c) and (d), “ghost” images are visible to the left of the nucleus about halfway between the nucleus and the ring, and these should be ignored. In (e) and (f) a cluster of ion spots is seen near the bottom of the frames, which should also be ignored.

PLATE 2

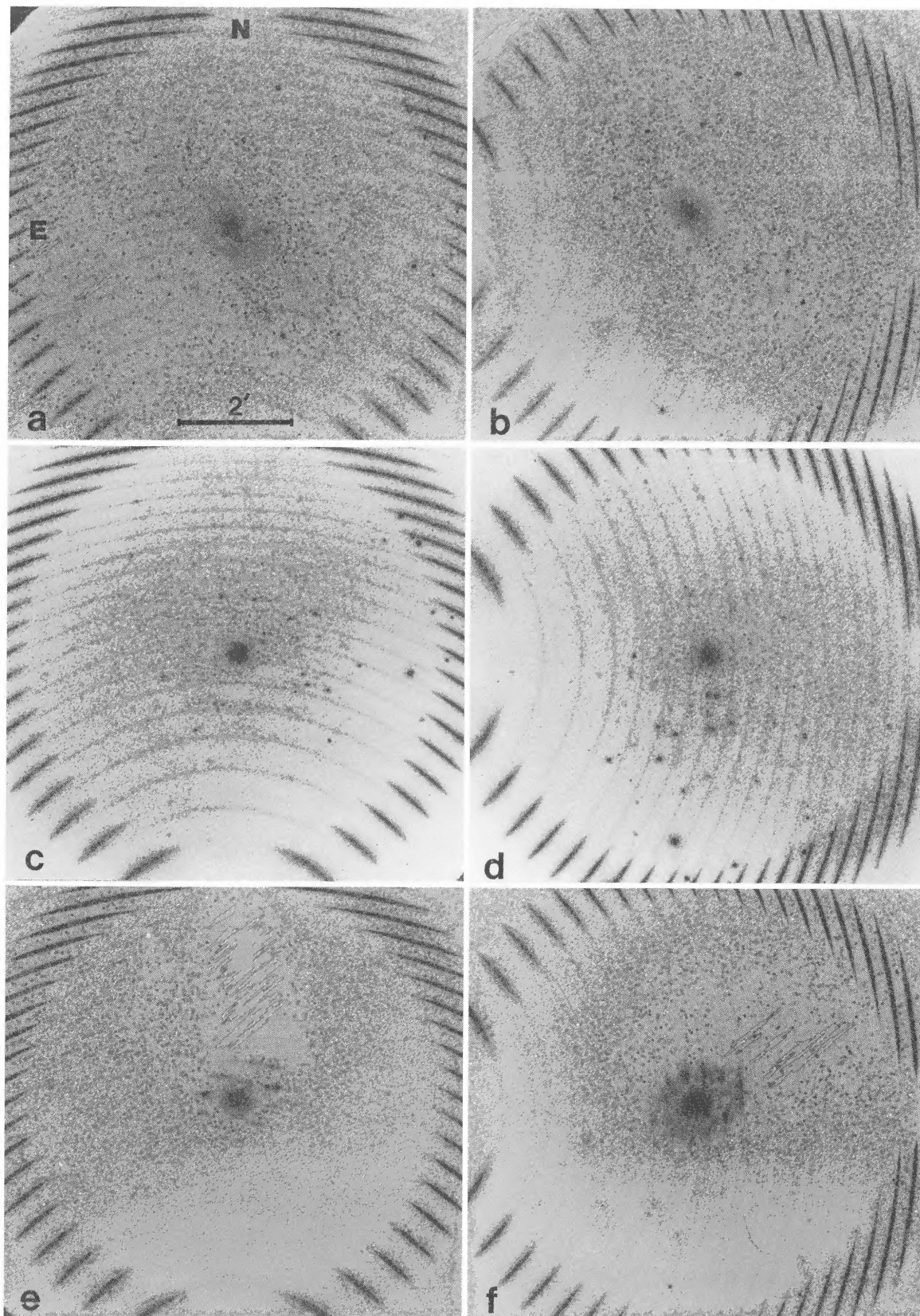


FIG. 2.—Examples of interferograms obtained with the McDonald Observatory Mark II interferometer. Top panels show NGC 4725, middle panels show NGC 3351, and bottom panels show NGC 4736. The left-hand panels were taken in a position angle of 0° , while the right-hand panels were taken in a position angle of 270° . Calibration fringes from a hydrogen calibration lamp surround each field, and some weak fringing due to night-sky OH lines is visible on all the images. The image in (*d*) has numerous bright ion spots below the nucleus of the galaxy which should be ignored. These same spots are also visible, though less conspicuously, in (*c*) to the right of the galaxy nucleus.

TABLE 1
BASIC PARAMETERS

Parameter	NGC 1512	NGC 3351	NGC 4725	NGC 4736
Coordinates				
(1) α (1950).....	04 ^h 02 ^m 3	10 ^h 41 ^m 3	12 ^h 48 ^m 0	12 ^h 48 ^m 5
(2) δ (1950).....	-43°29'	+11°58'	+25°47'	+41°24'
(3) l	248°7	234°0	295°1	123°4
(4) b	-48°2	+56°4	+88°4	+76°0
(5) SGL.....	-250°2	94°1	91°5	76°2
(6) SGB.....	-44°4	-27°1	+5°7	+9°5
Morphologies				
(7) RC2.....	SB(r)a	SB(r)b II	SAB(r)abp I	(R)SA(r)ab II
(8) RSA.....	SBb(rs) Ip	SBb(r) II	Sb/SBb(r) II	(R)Sab(s)
(9) SGC.....	(R')SB(r)ap
Integrated Quantities				
(10) B_T	11.10±0.05	10.55±0.06	10.06±0.05	8.96±0.05
(11) $(B-V)_T$	0.80±0.02	0.80±0.03	0.76±0.05	0.75±0.04
(12) $(U-B)_T$	0.10±0.04	0.20±0.04	...	0.16±0.04
(13) $\log A_e$	1.36±0.02	1.34±0.03	1.54±0.04	1.13±0.03
(14) m'_e (mag min ⁻²).....	13.39	12.74	13.25	10.10
Orientations				
(15) θ_0 (photometry).....	37° (B81)	319°: (K87)
(16) θ_0 (optical kinematics).....	263°±1°	193°±1°	27°±5°	295°±1°
(17) θ_0 (H I kinematics).....	265° (H79)	...	30° (W84)	302° (B77)
(18) i	35°±5° (H79)	40° (R75)	50°±5° (RC2, B81)	35°±3° (RC2, K87)
Rings				
(19) d_r (arcmin).....	2.40	2.19	4.35	1.65
(20) d_r (kpc).....	12	7	14.5	3
(21) θ_r	231°	190°	40°	305°
(22) q_r	0.77	0.86	0.55	0.73
(23) θ_{Br}	10°	80°	10°	...
Kinematics				
(24) V_{sys} (km s ⁻¹).....	889±2	772±3	1188±6	310±2
(25) V_m (km s ⁻¹).....	219:	227	248:	194
Distances				
(26) μ_0	31.1±0.5	30.2±0.3	30.3±0.3	29.0±0.5

PARAMETERS.—(1–7) Right ascension, declination, Galactic coordinates, supergalactic coordinates, and revised Hubble type and luminosity class from RC2; (8) type and luminosity class from Sandage and Tammann 1981; (9) type from Corwin, de Vaucouleurs, and de Vaucouleurs 1985; (10–14) integrated magnitude, integrated colors, effective aperture, and mean effective surface brightness from multiaperture photoelectric photometry; (15) major-axis position angle from surface photometry (see references below); (16) major-axis position angle (receding half) from optical kinematics, assuming circular rotation; (17) major-axis position angle (receding half) from H I kinematics (references below); (18) adopted inclination (references below); (19–22) apparent diameter, linear diameter, major-axis position angle, and apparent axis ratio of the inner ring; (23) apparent relative angle between bar and inner ring; (24) systemic velocity from new interferometer data; (25) maximum rotation velocity; (26) distance modulus (Buta 1984).

KEY TO REFERENCES.—B77: Bosma, van der Hulst, and Sullivan 1977 (inner regions); B81: Boroson 1981; H79: Hawarden *et al.* 1979; K87: Kent 1987 and S. M. Kent 1987, private communication; RC2: de Vaucouleurs, de Vaucouleurs, and Corwin 1976; R75: Rubin, Ford, and Peterson 1975; W84: Wevers *et al.* 1984 (inner regions).

TABLE 2
PHOTOELECTRIC PHOTOMETRY OF NGC 1512

<i>A</i>	log <i>A</i> (0.1)	<i>V</i>	<i>B</i> - <i>V</i>	<i>U</i> - <i>B</i>	(<i>V</i> - <i>R</i>) _J	(<i>R</i> - <i>I</i>) _J	Notes
33.3	0.74	12.22	0.88	0.22	0.84	0.69	
65.8	1.04	11.68	0.89	0.29	0.85	0.67	
98.8	1.22	11.34	0.89	0.30	0.84	0.69	
131.1	1.34	11.07	0.87	0.28	0.84	0.67	1
131.1	1.34	11.04	0.86	0.28	0.77	...	1
253.0	1.62	10.48	0.84	0.03	1
16.2	0.43	14.61	1.15	1.00	1.11	0.73	2
16.2	0.43	14.54	1.21	1.04	1.09	...	2

NOTES.—(1) Corrected for star A. (2) Star A.

TABLE 3A
LOG OF McDONALD FABRY-PEROT INTERFEROGRAMS

RC-FP2	Object (NGC)	P.A.	Exposure Time (minutes)	Date 1981	RC-FP2	Object (NGC)	P.A.	Exposure Time (minutes)	Date 1981
114	3351	270°	45	Mar 8	137	4725	225°	45	Apr 5
115	3351	0	45	Mar 8	138	4736	270	45	Apr 5
116	4725	0	45	Mar 8	139	4736	0	45	Apr 5
117	4725	270	45	Mar 8	140	4736	0	10	Apr 5
118	4736	270	32	Mar 8	142	3351	225	60	Apr 7
119	4736	0	13	Mar 8	143	3351	315	60	Apr 7
133	3351	225	45	Apr 5	145	4725	270	60	Apr 7
134	3351	315	45	Apr 5	146	4725	0	60	Apr 7
136	4725	315	45	Apr 5					

TABLE 3B
LOG OF McDONALD INTERFERENCE FILTER PHOTOGRAPHS

RC-IFP	Object (NGC)	Exposure Time (minutes)	λ (Å)	Hα	Date 1981
007	3351	30	6581	ON	Mar 5
009	3351	30	6570	OFF	Mar 5
015	4725	30	6586	ON	Mar 5
017	4725	30	6575	OFF	Mar 5
027	4736	30	6570	ON	Mar 7
029	4736	30	6581	OFF	Mar 7

errors appear to be about 16 km s^{-1} per velocity point. The comparison with the PRFT data suggests external errors closer to 20 km s^{-1} for NGC 3351, and this is probably also representative of the data for NGC 4725.

It was also found that there is a small but significant systematic zero-point difference between the Mark II data and the other data sets, the average difference being $\sim -8 \pm 3 \text{ km s}^{-1}$. The systemic velocities obtained with the published data sets agree better with fairly precise radio radial velocities, and hence indicate that the systematic error is probably in the Mark II data. Table 1 summarizes the new systemic velocities, but in the analysis of §§ V and VI velocities from the Mark II interferometer will be adjusted in zero point to

agree with the other sets (excepting NGC 4736, where the difference was found to be only marginally significant).

The IDS observations of NGC 4725 were obtained by M. L. McCall and myself in 1981 May. The H II regions, their radial velocities, and several other parameters are compiled in Table 4. H II regions were chosen on the basis of the H α photograph in Figure 1a. Positions were measured relative to SAO stars and secondary position standards set up in the field in and around NGC 4725. At the telescope, most of the H II regions were not visible on the TV monitor and had to be found by offsetting with precise relative coordinates from a nearby field star.

Details of the reduction and analysis of the spectra are given by Buta (1984). Internal errors in the resulting velocities were found to be less than 10 km s^{-1} , based on objects observed on more than one night. Zero-point errors are less than 5 km s^{-1} , based on two stars from the *General Catalogue of Stellar Radial Velocities* (Wilson 1953), used as standards. It was found that the velocities also agree well with those obtained with the Mark II interferometer, except for a small zero-point difference. The sense of the difference was found to be consistent with the other comparisons.

Finally, observations of NGC 1512 were made using the TAURUS Fabry-Perot interferometer (Taylor and Atherton 1980) attached to the 3.9 m Anglo-Australian Telescope. Details of the reductions are the same as for NGC 1433, described by Buta (1984) and in Paper II. The external errors

TABLE 4
RADIAL VELOCITIES OF H II REGIONS IN THE INNER RING OF NGC 4725 FROM McDONALD IDS OBSERVATIONS

Object Name (1)	P.A. (1950) (2)	r (3)	V_{\odot} (km s^{-1}) (4)	$\frac{F(\text{H}\alpha)}{F([\text{N II}])}$ (5)	$10^{14} F(\text{H}\alpha)$ ($\text{ergs cm}^{-2} \text{s}^{-1}$) (6)
NGC 4725 1	63°0	99".5	1313	3.1 ± 0.7	3.00
NGC 4725 2	20.3	123.5	1365	2.8 ± 0.3	1.98
NGC 4725 3	345.3	81.0	1309	2.6	1.13
NGC 4725 4	315.8	74.1	1235	2.5	0.88
NGC 4725 5	287.0	82.2	1176	4.8 ± 0.9	0.31
NGC 4725 6	259.0	102.0	1141	3.6 ± 0.3	0.88
NGC 4725 7	250.0	118.5	1111	3.5 ± 0.3	0.68
NGC 4725 8	242.0	124.9	1086	4.0 ± 0.1	0.80
NGC 4725 9	232.0	125.2	1045	3.0 ± 0.3	0.70
NGC 4725 10	207.0	127.2	1000	2.6 ± 0.4	0.95

Col. (1).—Arbitrary designation.

Col. (2).—Position angle relative to optical nucleus.

Col. (3).—Radius from nucleus.

Col. (4).—Heliocentric radial velocity.

Col. (5).—Ratio of flux in $\text{H}\alpha$ to flux in $[\text{N II}] \lambda 6583$.

Col. (6).—Flux in $\text{H}\alpha$.

of the TAURUS velocities were assessed in Papers II and III from comparisons with independently derived slit spectrum velocities and are of the order of $13\text{--}15 \text{ km s}^{-1}$ per velocity point in a $1''.30 \times 1''.30$ cell, after application of a three-dimensional smoothing process. The observations of NGC 1512 were obtained under similar conditions and with similar parameters to those for the other galaxies, and these errors should be representative.

Figures 3*a*–3*d* show the distributions of velocity points for the four galaxies from the new observations and including the published data where available. As for NGC 1433, the distributions of discrete H II regions in NGC 1512, NGC 3351, and NGC 4725 are confined largely to a ringlike pattern coinciding with the blue-light inner ring in each case. The distribution is broad on the southwest side in NGC 4725 owing to spiral structure just outside the inner ring. In the center of NGC 1512, a clear nuclear ring of gas is present that is slightly asymmetrically centered on the nucleus and which has a different shape and position angle compared with the inner ring distribution. In NGC 4736 most emission is concentrated within the inner ring, and only very much fainter discrete H II regions provide velocities outside it. In addition to the published data of van der Kruit (1976*a*), Figure 3*d* shows the velocity points obtained by Chincarini and Walker (1967), which provide fairly precise velocity information within the inner ring of NGC 4736. These velocities are based on a combination of absorption- and emission-line measurements. Additional absorption-line measurements along the major axis of NGC 4736 were made by Pellet and Simien (1982), but these cover a more limited range in radius.

IV. VELOCITY FIELDS

The velocity field of each galaxy is shown in Figures 4*a*–4*e*. For NGC 1512 and NGC 4725, the coverage is too sparse to see the details of the global velocity field well, but at least for NGC 1512 it appears that the velocity gradient is not

along the apparent major axis of the inner ring (which is nearly coincident with the bar axis). The nuclear region velocity field of NGC 1512, shown at high resolution in Figure 4*b*, displays greater regularity than that in NGC 1433 but shows clear evidence for probable noncircular motions in the southeast quadrant, where a major dust lane cuts across the ring (see Lindblad and Jorsater 1981). A similar though weaker pattern is visible in the northwest quadrant, where an opposing dust lane crosses the ring.

The velocity field of NGC 3351 was obtained by combining the Mark II interferometer data with the PRFT and Rubin, Ford, and Peterson (1975) data assuming equal weights and after applying a zero-point correction of $+7.5 \text{ km s}^{-1}$ to the Mark II velocities. Apart from some probable noise in the northeast quadrant, the inner ring of this galaxy displays a regular velocity field. The slight bending of the contours as they cross into the nuclear region on the east side may be indicative of noncircular motions (Rubin, Ford, and Peterson 1975).

The velocity field of NGC 4736 is displayed in Figure 4*e*. The galaxy field has been divided into $5'' \times 5''$ cells, and interpolation has been performed for some cells. Equal weights were given to the three available data sets. Before construction of the map, the data of Chincarini and Walker (1967) were corrected for the significant zero-point errors derived by van der Kruit (1976*b*). Near the minor axis the velocity field is fairly regular; there is only a weak sign that the contours bend as they cross the inner ring. On the southeast side, there is, however, an obvious unusual field: the contour for 210 km s^{-1} is nearly straight, which is inconsistent with uniform circular motions for a radial position so far from the minor axis of the galaxy. The corresponding contour on the opposite side, for $V = 410 \text{ km s}^{-1}$, looks more normal. This asymmetry was also found by van der Kruit (1976*b*) and is confirmed to fairly high precision with the new Mark II interferometer data.

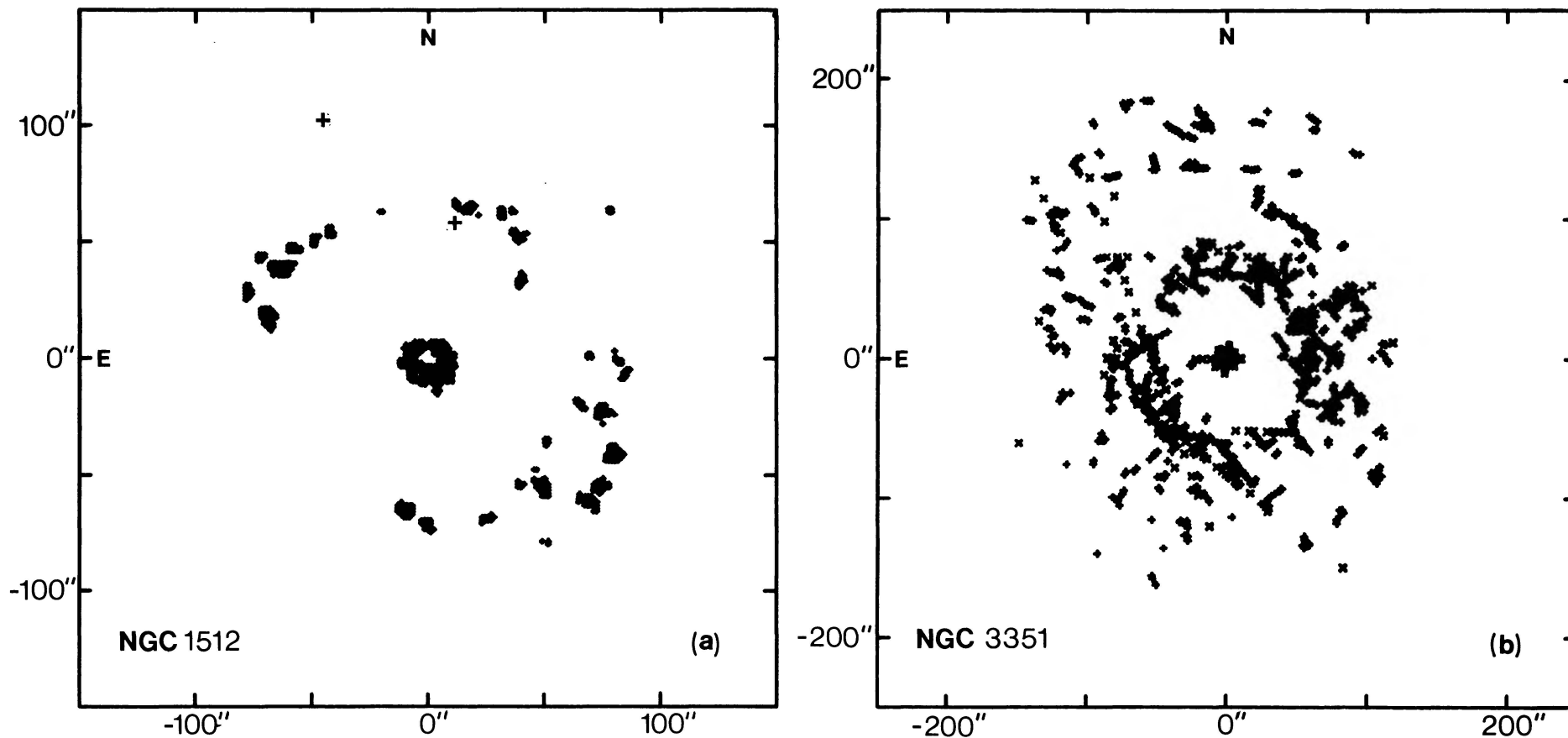


FIG. 3.—The distributions of velocity points based on the new velocity observations given in this paper and on published observations. For NGC 1512 the points are from TAURUS observations alone. For NGC 3351 small crosses indicate points from PRFT and Rubin, Ford, and Peterson (1975), while the plus symbols in this case and in NGC 4725 and 4736 denote points from Mark II interferometer data. For NGC 4725, Large open circles denote points from IDS spectroscopy, while for NGC 4736 small crosses are points taken from van der Kruit (1976*a*) and Chincarini and Walker (1967). A few field stars are indicated by the large plus signs in the panels for NGC 1512 and 4725. The nucleus position of NGC 4725 is also indicated.

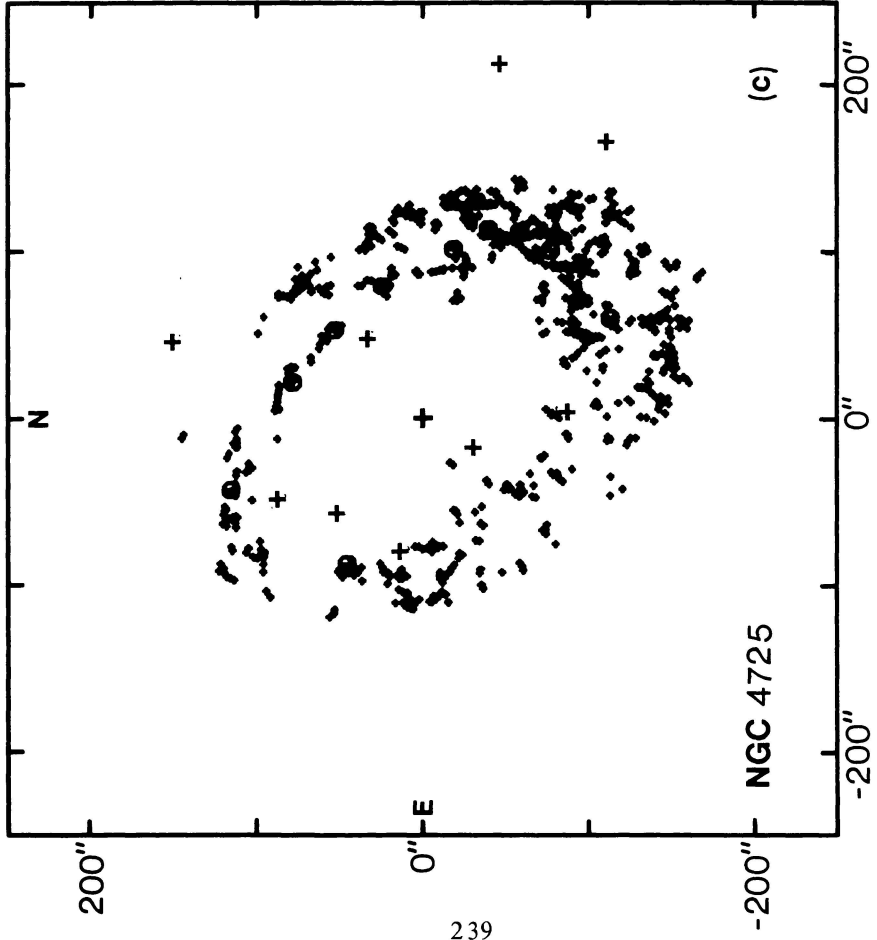
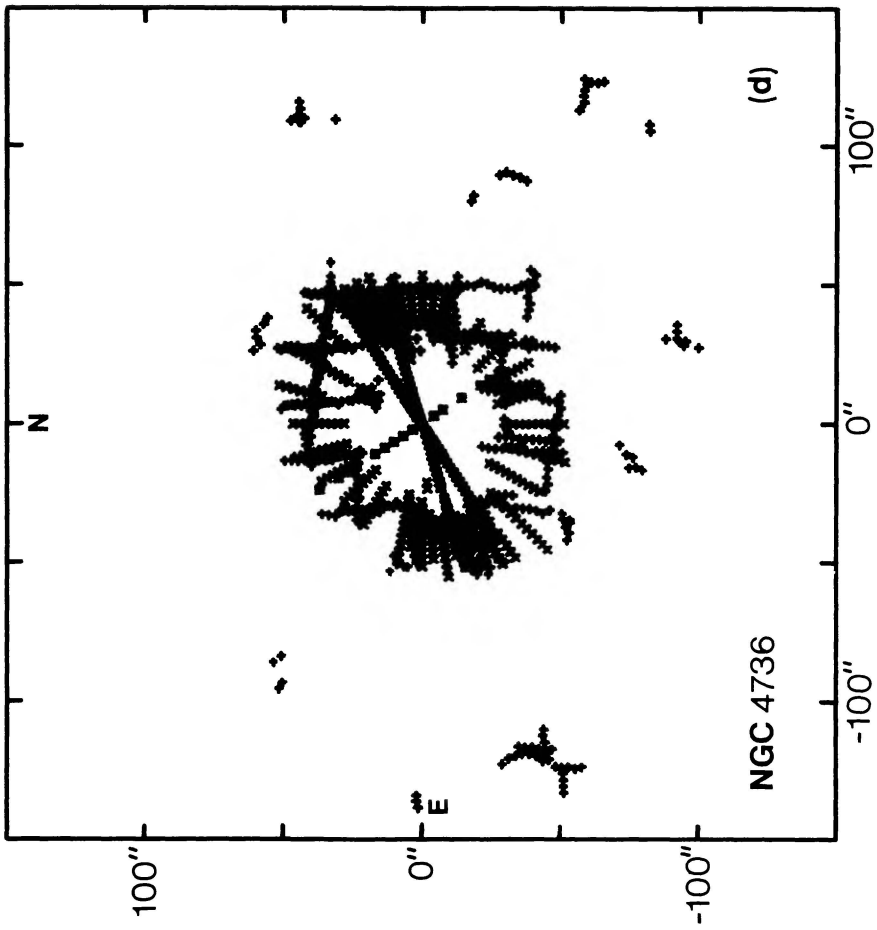


FIG. 3—Continued

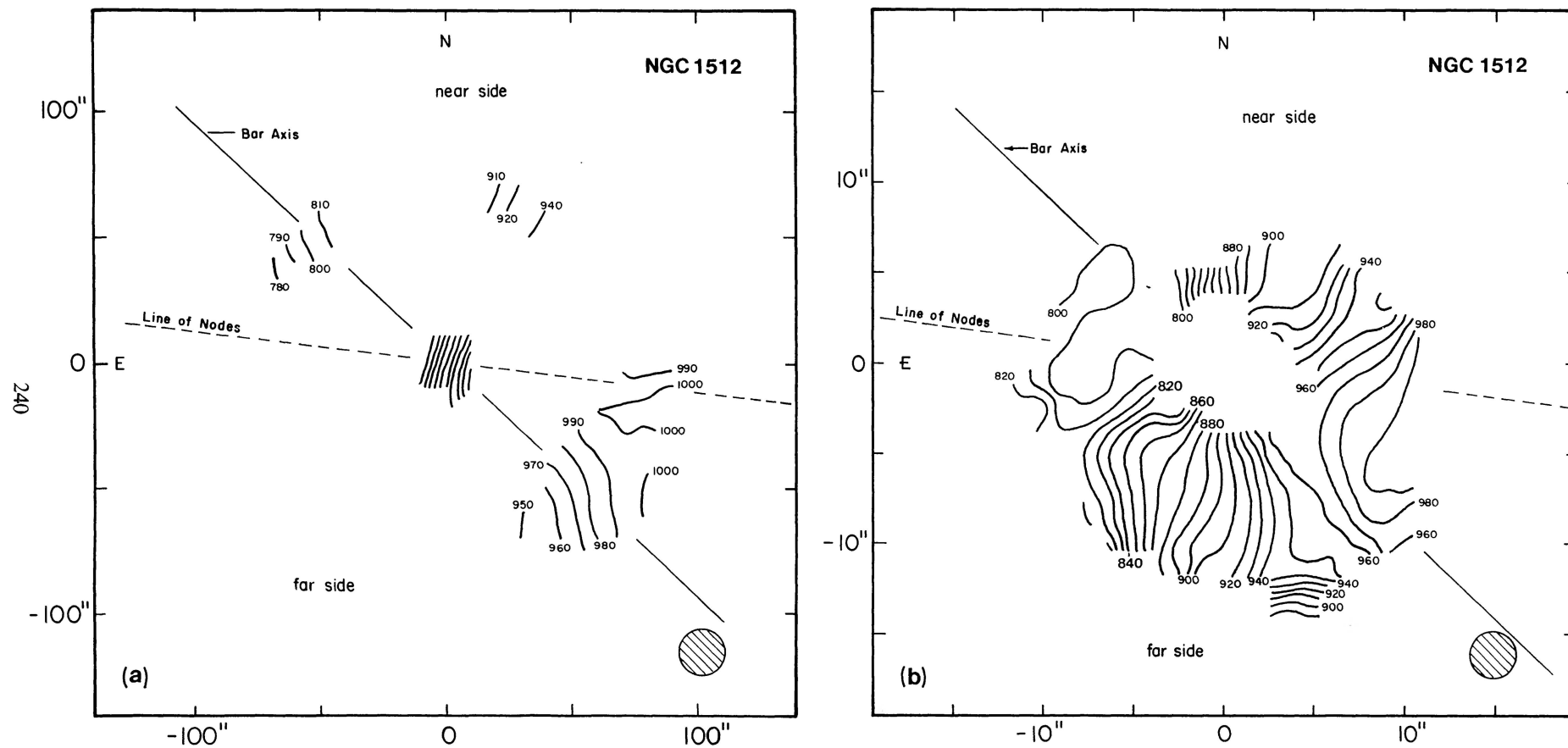


FIG. 4.—Velocity fields. The line of nodes for circular rotation is shown for each case, as well as the position angle of the bar for NGC 1512 and 3351. The line of nodes for the expanding ring model of NGC 4725 is also shown. Judgments of the near- and far-side positions are indicated for each case, based on the velocities and inspection of photographs assuming trailing spiral structure and noting the dust distribution.

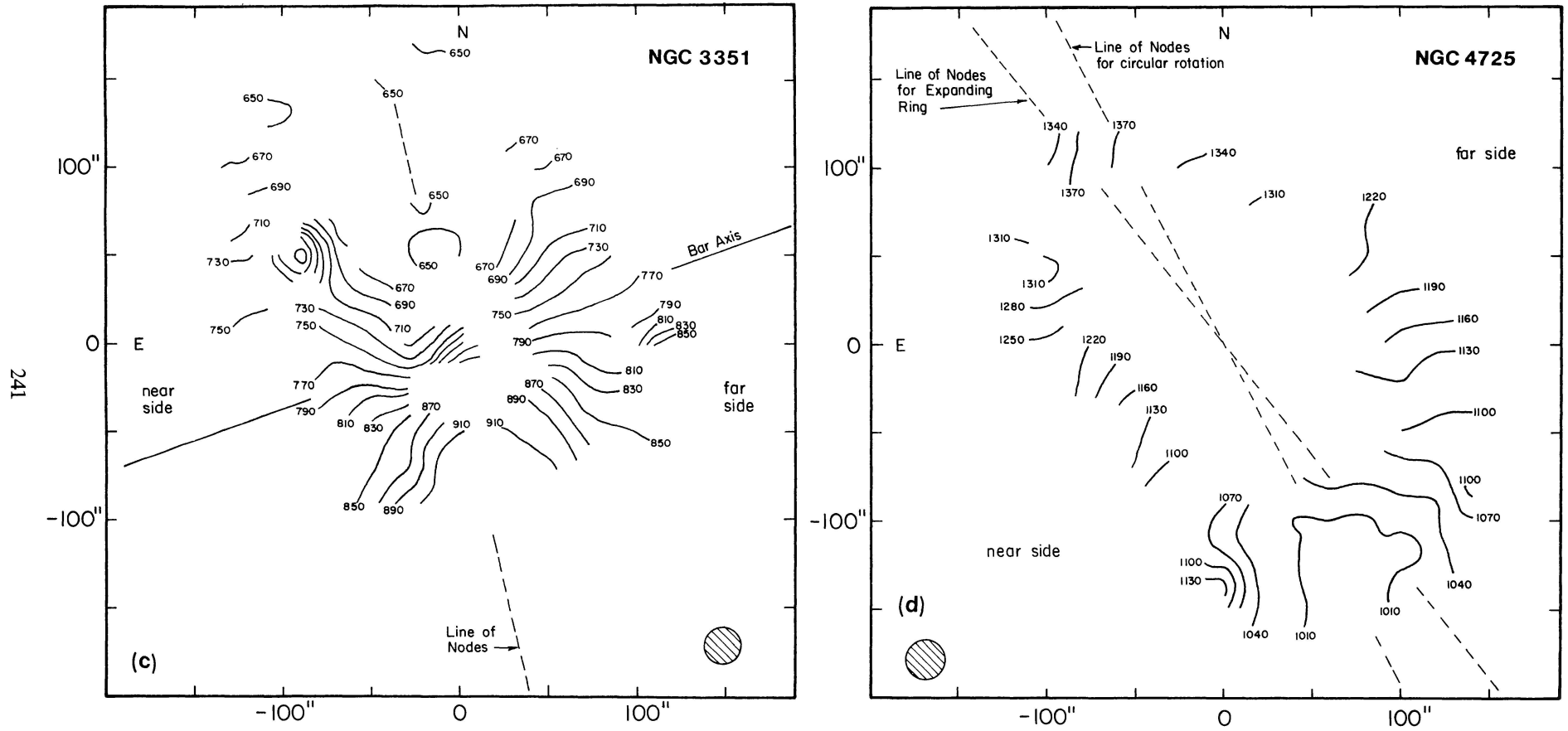


FIG. 4—Continued

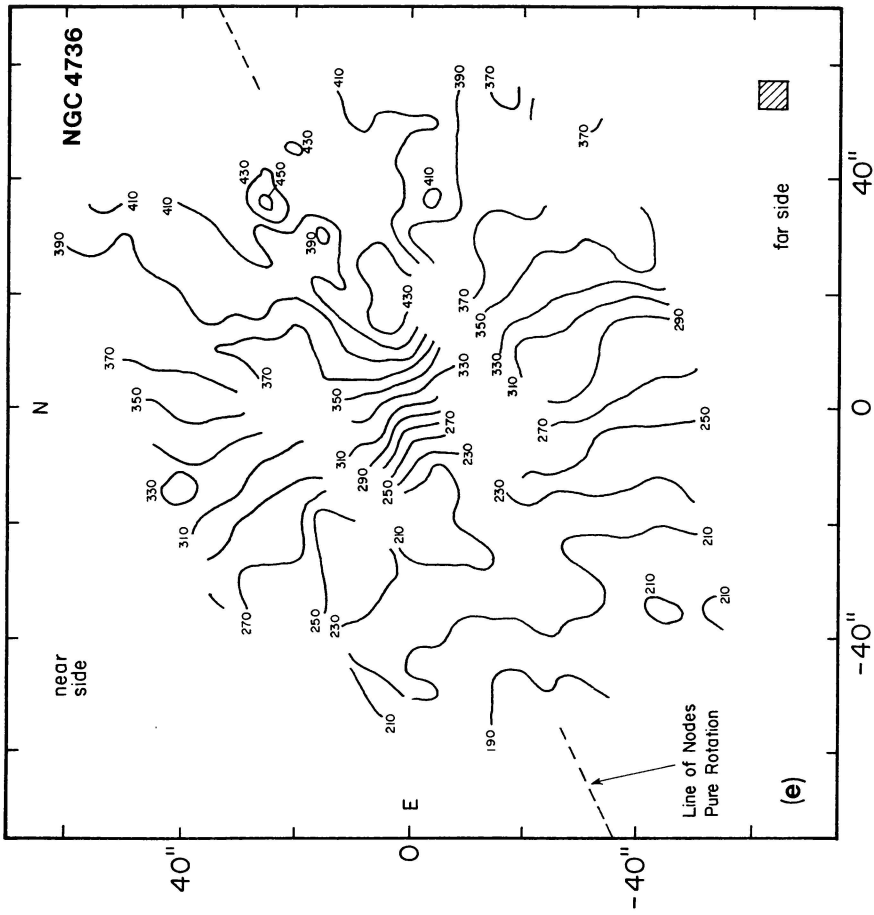


FIG. 4—Continued

V. ROTATION CURVES, MASSES, AND MASS-TO-LIGHT RATIOS

Using all of the available velocity data points (new plus previously published), rotation curves were derived for each galaxy under the assumption that the motions in the plane are predominantly circular. The iterative procedure described by Warner, Wright, and Baldwin (1973, hereafter WWB) and Davoust and de Vaucouleurs (1980) was used for this purpose, and in general only points within 40° – 45° of the major axis were used. For none of these galaxies could the inclination be determined very reliably from this method. Axis ratios from published surface photometry or from the RC2, or inclinations from other sources, are used instead. These are summarized for each galaxy in Table 1. Further discussions can be found in Buta (1984).

The rotation curves are illustrated in Figures 5*a*–5*d* and are compiled in Tables 5–8. There is reasonable symmetry between the two halves of the major axis for NGC 1512, NGC 3351, and NGC 4725, and for this reason Tables 5–7 present only the folded rotation curves. Noteworthy characteristics of NGC 1512 are the rapid rise to maximum velocity in the nucleus, and the more or less constant velocity across the inner ring region. Similar characteristics have been observed in other barred spirals, such as NGC 1097 (Schempp and Wolstencroft 1979), NGC 1300 (Peterson and Huntley 1980), and NGC 1433 (Paper II). A similar trend is also apparent in NGC 3351, except that the maximum velocity is not achieved at the edge of the optical emission in the nucleus.

For NGC 4736, the rotation curve is unusual across the inner ring region. The striking asymmetry apparent in the velocity field appears in the form of constant rotation velocity across the ring on the northwest side, and a steep linear rise in velocity across the ring on the southeast side. The different data sets (especially the Mark II and van der Kruit sets) were found to be in such good agreement on the trend that the mean error bars in the ring region are smaller than the symbols used for the plotted points (i.e., less than 5 km s^{-1}). Because of the asymmetry, I have not folded the rotation curve; Table 8 summarizes the results for the two sides separately. There is good agreement between the two sides for $r < 30''$ and for $r > 75''$, the difference being manifested *only* in the ring region $30'' < r < 65''$. The two curves in this region, when folded about the center, intersect at $r \sim 46''$, which is close to the ridgeline H α radius of the ring measured by van der Kruit (1976*b*).

The origin of the asymmetry is unclear. Van der Kruit (1976*b*) has favored the view that some aspects of the kinematics of this region are best explained by an explosive origin of the ring (see also Garman and Young 1986), while Schommer and Sullivan (1976) have favored the interpretation of the ring in terms of an inner Lindblad resonance, although neither model should predict an asymmetry of the kind observed. Since the slope may be due to a gasdynamical effect (for example, the self-gravity of the ring may be responsible for the trend), for the purpose of mass modeling only the velocities from the northwest side of the ring will be used.

Tables 9 and 10 compile parameters (masses and mass-to-light ratios) of several rotation curve models fitted to the data. For NGC 1512, NGC 3351, and NGC 4736, a combination of inhomogeneous spheroids having a polynomial density distribution of index $n = 2$ (Perek 1962) was used to obtain the mass within the maximum radius, r_t , covered by the optical rotation curves. In all cases, it was not possible to represent the rotation curves with only two spheroids, but three were needed for NGC 1512 and NGC 3351, and four were needed for NGC 4736 when radio data (Bosma, van der Hulst, and Sullivan 1977) are used for the outer parts (Fig. 6*a*). Owing to the gaps in the data between the rings, such models necessarily can only be regarded as illustrative. For NGC 4725, no sophisticated models could be applied. Instead, the point-mass approximation was used to obtain an initial mass estimate, and then a correction was applied to this estimate to make it consistent with the others. The correction $\langle M_0(r_t)/M_p(r_t) \rangle = 1.46$, based on seven objects (including NGC 1433, NGC 6300, and NGC 7531 from Papers II–IV), was used to reduce the point mass M_0 to the system of the flattened spheroids M_p .

To obtain the mass-to-light ratios, integrated luminosities were derived from multiaperture photometry (Longo and de Vaucouleurs 1983). This method would be fairly precise if the galaxies were all face-on, and since none is very highly inclined, we commit no serious error by ignoring the inclination effect on the isophotes. The resulting mass-to-light ratios have been corrected for Galactic extinction, internal absorption, and redshift according to RC2 procedures. The results show that NGC 1512, NGC 3351, and NGC 4725 have (on the zero point of de Vaucouleurs's distance scale) $(M/L)_B \sim 4$ – 6 , reasonably typical (Faber and Gallagher 1979), but for NGC 4736 the ratio is only about 1–2. While an overestimate of the distance to NGC 4736 by a factor of ~ 4 could explain this difference, the more likely cause is the unusually high surface brightness of the inner regions (Table 1). This low mass-to-light ratio was also found for NGC 4736 by Dufloot (1962).

An additional mass model which could only be applied to NGC 4736 is a finite velocity dispersion model (Davoust and de Vaucouleurs 1980). The most reasonable of such models is shown in Figure 6*b*, the parameters being compiled in Table 10. The model is of a two-component nature, and a useful check of its sensibility is to compare the central velocity dispersion required by the model with actual measurements such as those, for example, made by Whitmore, Kirshner, and Schechter (1979), who obtained $\sigma_v(0) = 134 \pm 17 \text{ km s}^{-1}$. The central velocity dispersion in the adopted model is $\sigma_v(0) = 145 \text{ km s}^{-1}$, in reasonable agreement with the measured value. The flattening of the spheroid, 0.45, is a weakness of the model, since the very nearly round isophotes in the bulge do not support such a low value. The true flattening of the bulge is probably not less than 0.75. The mass-to-light ratio of each component in this model was estimated using the relation of Simien and de Vaucouleurs (1986), which gives the relative magnitude, $\Delta m_p^0(B)$, of the bulge to the total magnitude of the galaxy as a function of galaxy type. On average, this magnitude difference is 1.23 mag for Sab galaxies, and leads to the mass-to-light ratios given in Table 10.

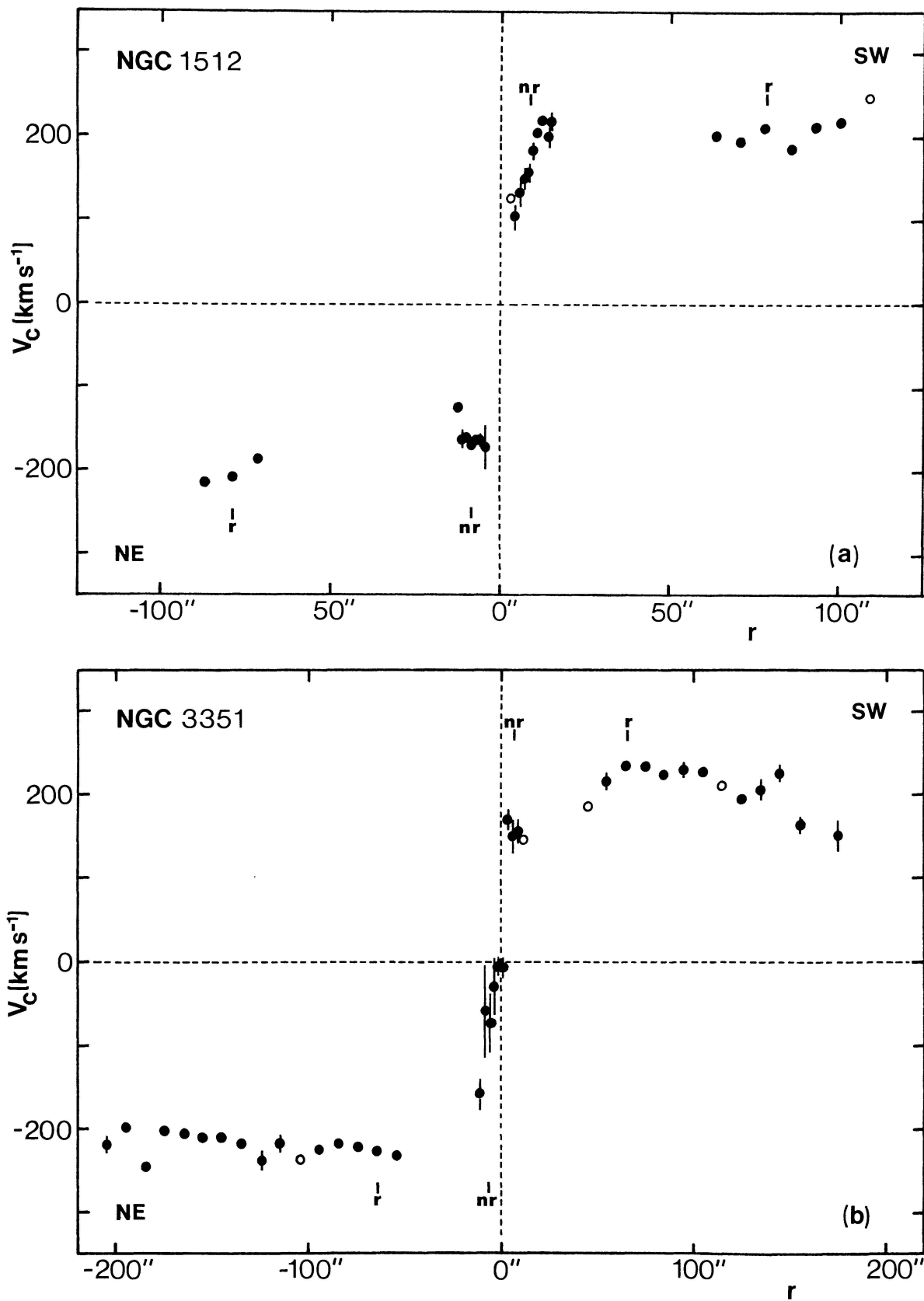


FIG. 5.—Rotation curves assuming pure circular rotation. Points based on only a single measurement are indicated by open circles. The panel for NGC 4725 is especially uncertain, since the assumption of pure circular rotation is definitely incorrect for this object. Positions of inner rings (r) and nuclear rings (nr) are indicated.

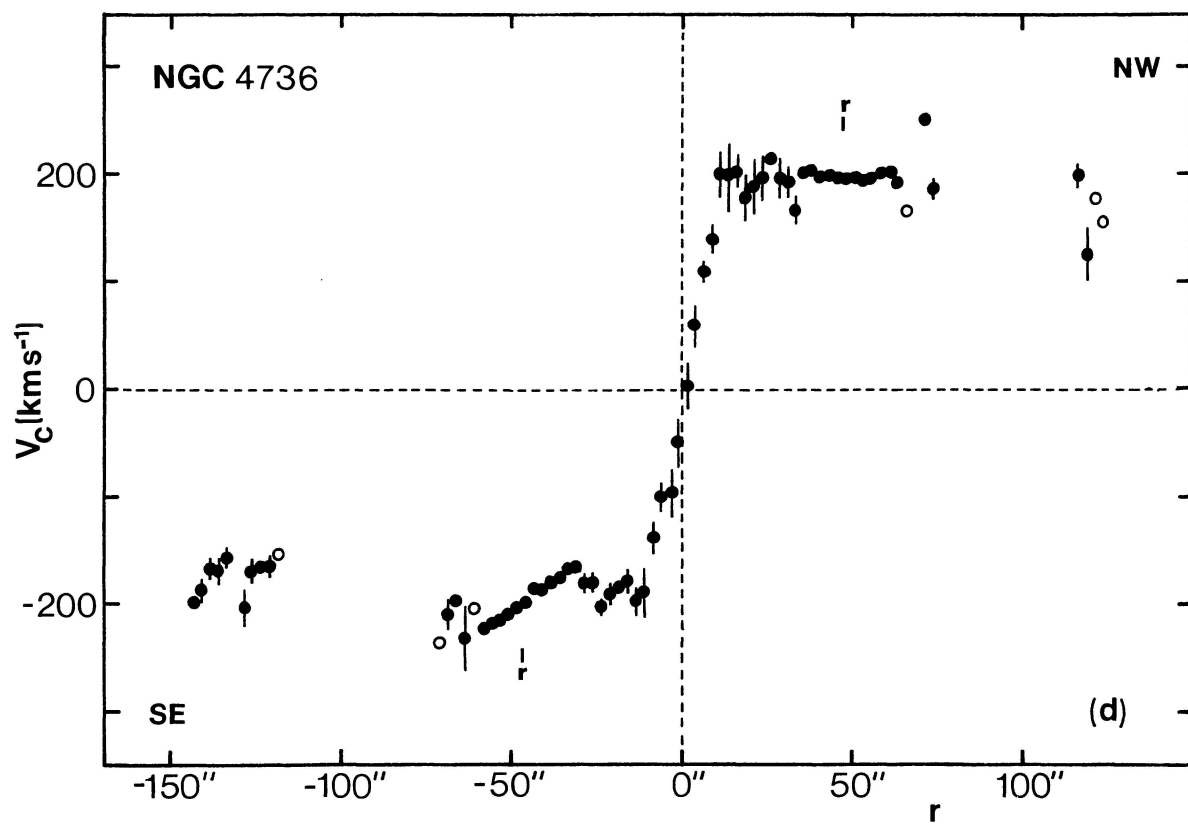
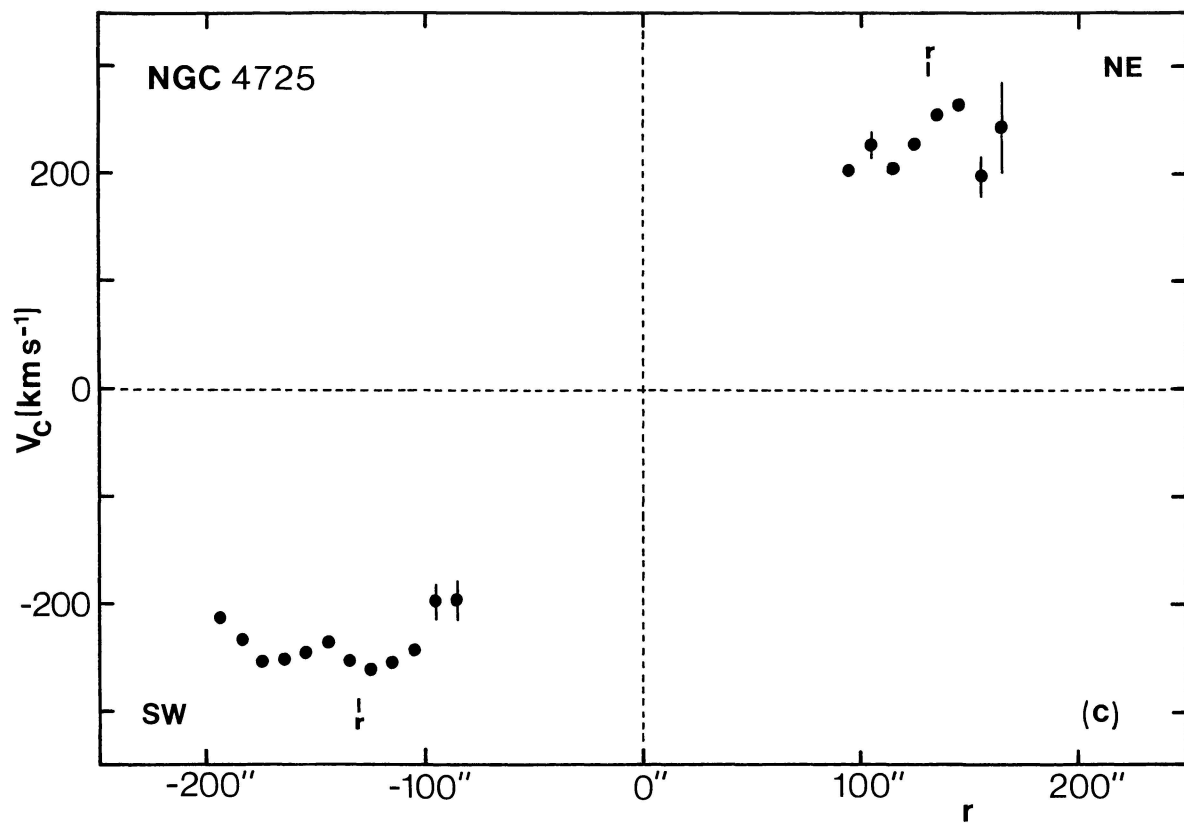


FIG. 5—Continued

BUTA

TABLE 5
ROTATION CURVE OF NGC 1512

r (1)	V_c (2)	N (3)	σ_1 (4)	m.e. (5)	r (1)	V_c (2)	N (3)	σ_1 (4)	m.e. (5)
3.25.....	125.5	1	13.65	200.8	2	19.5	13.8
4.55.....	139.5	7	53.7	20.3	14.95	218.4	3	16.9	9.7
5.85.....	153.5	10	16.8	5.3	63.75	203.5	7	8.5	3.2
7.15.....	165.8	11	15.5	4.7	71.25	188.2	48	15.9	2.3
8.45.....	163.1	17	26.6	6.5	78.75	209.6	63	8.5	1.1
9.75.....	168.9	21	22.4	4.9	86.25	213.7	32	17.6	3.1
11.05.....	186.6	16	25.6	6.4	93.75	214.0	29	9.0	1.7
12.35.....	181.9	8	50.9	18.0	101.50	219.2	27	25.9	5.0

Col. (1).—Radius in galaxy plane (arcsec).

Col. (2).—Mean rotational velocity (km s^{-1}), assuming pure circular motion.

Col. (3).—Number of points in mean.

Col. (4).—Standard deviation about mean (km s^{-1}).

Col. (5).—Mean error of mean.

TABLE 6
ROTATION CURVE OF NGC 3351

r (1)	V_c (2)	N (3)	σ_1 (4)	m.e. (5)	r (1)	V_c (2)	N (3)	σ_1 (4)	m.e. (5)
1.25.....	15.5	25	75.3	15.1	105.00	223.6	16	14.2	3.5
3.75.....	100.3	6	86.6	35.3	115.00	217.6	20	34.0	7.6
6.25.....	129.8	6	7.7	3.2	125.00	234.0	21	41.0	8.9
8.75.....	105.9	4	73.4	36.7	135.00	203.9	15	17.9	4.6
11.25.....	154.1	3	20.2	11.7	145.00	222.3	31	27.8	5.0
45.00.....	186.0	1	155.00	193.2	24	35.9	7.3
55.00.....	225.6	27	25.9	5.0	165.00	204.4	16	11.0	2.7
65.00.....	228.9	89	19.2	2.0	175.00	198.2	31	37.5	6.7
75.00.....	223.3	83	17.6	1.9	185.00	244.9	12	10.3	3.0
85.00.....	225.3	34	21.4	3.7	195.00	198.0	13	12.2	3.4
95.00.....	236.3	14	18.7	5.0	205.00	218.4	6	19.3	7.9

NOTE.—Columns as in Table 5.

TABLE 7
ROTATION CURVE OF NGC 4725

r (1)	V_c (2)	N (3)	σ_1 (4)	m.e. (5)	r (1)	V_c (2)	N (3)	σ_1 (4)	m.e. (5)
85.0.....	195.1	5	38.9	17.4	145.0	239.4	55	21.3	2.9
95.0.....	197.0	11	47.0	14.2	155.0	247.4	91	21.5	2.3
105.0.....	239.7	33	21.2	3.7	165.0	249.2	53	19.8	2.7
115.0.....	248.8	39	22.6	3.6	175.0	252.2	32	12.3	2.2
125.0.....	254.4	65	25.2	3.1	185.0	232.6	17	12.9	3.1
135.0.....	253.9	62	19.8	2.5	195.0	211.8	7	14.9	5.6

NOTE.—Columns as in Table 5.

Finally, for NGC 4736, Kent (1987) has constructed a rotation curve model from the light distribution in the Thuan-Gunn r band. As is typical of many galaxies with extended H I rotation curves, a significant contribution from a massive dark halo is needed to reproduce the nearly constant velocities beyond the inner ring region.

VI. KINEMATICS AND DYNAMICS OF THE RINGS

As for NGC 1433, NGC 6300, and NGC 7531, the kinematics of the inner rings in the four galaxies here were studied by means of the velocity–position angle diagram (see van der

Kruit 1974, 1976*b*). This approach is useful because in each case the ring lies on the flat portion of the rotation curve, hence in any given position angle the rotation is nearly constant across the width of the ring. The curves are analyzed in terms of several very simple models: pure circular rotation, expanding or contracting ring, unperturbed dispersion orbit, or perturbed oval bar orbit (e.g., van der Kruit 1974, 1976*b*; Buta 1984; Wevers *et al.* 1984).

The perturbed oval bar orbit model that I use is the empirical one described in Paper II. Unfortunately, because NGC 1512 and NGC 4725 are interacting, the orientation

TABLE 8
ROTATION CURVE OF NGC 4736

r	V_c	N	σ_1	m.e.	r	V_c	N	σ_1	m.e.
1	2	3	4	5	1	2	3	4	5
1.25	3.5	4	41.0	23.6	-1.25	-49.5	2	32.5	23.0
3.75	60.1	3	31.8	18.4	-3.75	-96.7	6	59.1	24.1
6.25	110.4	7	21.6	8.2	-6.25	-99.6	7	35.9	13.6
8.75	140.1	5	29.3	13.1	-8.75	-137.5	4	31.7	15.8
11.25	199.9	5	43.5	19.5	-11.25	-188.4	4	49.1	24.5
13.75	197.5	3	56.0	32.3	-13.75	-196.4	3	23.2	13.4
16.25	201.7	5	31.3	14.0	-16.25	-177.8	4	23.8	11.9
18.75	177.6	4	42.2	21.1	-18.75	-184.0	2	5.0	3.5
21.25	188.9	4	52.7	26.3	-21.25	-190.1	4	22.6	11.3
23.75	196.5	7	54.0	20.4	-23.75	-202.4	3	13.6	7.9
26.25	213.8	8	18.6	6.6	-26.25	-179.6	2	11.3	8.0
28.75	196.4	5	41.5	18.5	-28.75	-180.8	5	17.5	7.8
31.25	191.7	14	51.4	13.7	-31.25	-165.1	11	25.1	7.6
33.75	166.1	18	48.5	11.4	-33.75	-165.9	15	19.1	4.9
36.25	200.9	25	22.6	4.5	-36.25	-174.5	23	11.8	2.5
38.75	203.1	19	14.7	3.4	-38.75	-179.5	27	21.5	4.1
41.25	196.6	21	12.7	2.8	-41.25	-184.7	25	19.3	3.9
43.75	198.8	22	16.4	3.5	-43.75	-185.6	22	16.8	3.6
46.25	197.4	26	10.7	2.1	-46.25	-198.2	22	15.1	3.2
48.75	194.4	30	13.6	2.5	-48.75	-203.2	19	8.9	2.1
51.25	197.0	33	13.8	2.4	-51.25	-208.3	19	14.5	3.3
53.75	194.2	22	13.1	2.8	-53.75	-215.5	16	22.0	5.5
56.25	197.1	15	12.8	3.3	-56.25	-217.9	12	27.5	7.9
58.75	200.8	9	19.1	6.4	-58.75	-224.2	9	19.4	6.5
61.25	201.3	9	20.7	6.9	-61.25	-202.2	1
63.75	190.0	4	7.4	3.7	-63.75	-231.4	2	44.3	31.3
66.25	165.4	1	-66.25	-195.6	2	1.4	1.0
71.25	250.8	3	13.5	7.8	-68.75	-208.6	4	28.6	14.3
73.75	184.9	2	13.3	9.4	-71.25	-234.9	1
88.75	131.6	1	-118.75	-152.2	1
91.25	136.7	1	-121.25	-164.4	2	13.0	9.2
113.75	102.8	1	-123.75	-165.7	6	13.4	5.5
116.25	198.6	2	15.4	10.9	-126.25	-169.0	8	29.8	10.5
118.75	124.5	5	56.4	25.2	-128.75	-202.2	3	28.4	16.4
121.25	178.6	1	-133.75	-156.0	4	14.6	7.3
123.75	155.5	1	-136.25	-168.6	3	22.2	12.8
					-138.75	-166.4	2	11.0	7.8
					-141.25	-187.2	2	13.2	9.3
					-143.75	-198.3	2	9.7	6.8

NOTE.—Columns as in Table 5.

TABLE 9
MASSES AND MASS-TO-LIGHT RATIOS FROM INHOMOGENEOUS
SPHEROID MODELS

Object (NGC)	r_l (kpc)	$M(r \leq r_l)$ ($10^{10} M_\odot$)	$f_0(B)$ ($\odot=1$)
(1)	(2)	(3)	(4)
1512.....	8.2	5.8	4.4
3351.....	10.9	7.9	5.7
4725.....	10.1	9.9	5.5
4736.....	3.9	1.9	1.1
4736.....	15.3	4.3	2.1

Col. (2).—Limiting radius for mass determination. Orientation parameters and distances used are given in lines 16, 18, and 26 of Table 1.

Col. (3).—Mass interior to r_l .

Col. (4).—Mass-to-blue light ratio corrected for Galactic extinction, internal absorption, and redshift.

TABLE 10
PARAMETERS OF FINITE VELOCITY DISPERSION MODEL OF NGC 4736^a

Parameter	Value	Parameter	Value
A. Spheroid		B. Disk	
a_1 (kpc)	0.19	a_2 (kpc)	8.32
b (kpc)	0.15	b (kpc)	0.15
c_1/a_1	0.45	c_2/a_2	0.02
M_1	1.35	M_2	3.58
\mathcal{L}_1	6.61	\mathcal{L}_2	1.39
f_{01} ($\odot=1$)	2.0	f_{02} ($\odot=1$)	2.6

^a \mathcal{L}_1 and \mathcal{L}_2 are derived from $B_T^0 = 8.63$ with $\Delta m_T(B) = 1.23$ (Simien and de Vaucouleurs 1986). Model is based on distance modulus $\mu_0 = 29.0$, and \mathcal{L} and M are in solar units $\times 10^{10}$. The parameters a , b , and c/a refer to length scales and flattenings of the components.

parameters are sufficiently uncertain that this kind of model cannot be used to make an independent estimate of the bar pattern speed, as was done for NGC 1433. It is a fair criticism to state that neglect of the effects of these interactions necessarily leads to oversimplification and uncertainty in these models, and may vitiate completely the simple approach being used. However, the models are not intended to be anything more than useful explorations of ring kinematics, because the optical data do not provide adequate information on the global velocity fields. Therefore, orientation parameters have been chosen which give a resonance parameter (see Paper II) $1 - \Omega_p/\Omega \sim 0.35$ (Ω = mean circular angular veloc-

ity), consistent with the interpretation (to first order) that the rings are linked with inner second harmonic resonance $2HR^-$ (Schwarz 1979, 1984b). The adopted models are summarized in Table 11. In addition to the kinematic parameters, Table 11 also gives a number of other useful parameters highlighted in Paper II, such as the maximum amplitude of the tangential force and the predicted position of corotation (CR) assuming constant rotation velocity across the disk. The tangential forces estimated by this kind of model range from 7% to 12% of the mean axisymmetric force, and although the estimates cannot be regarded as very reliable, these values are not unreasonable according to recent models (e.g., Schwarz 1979).

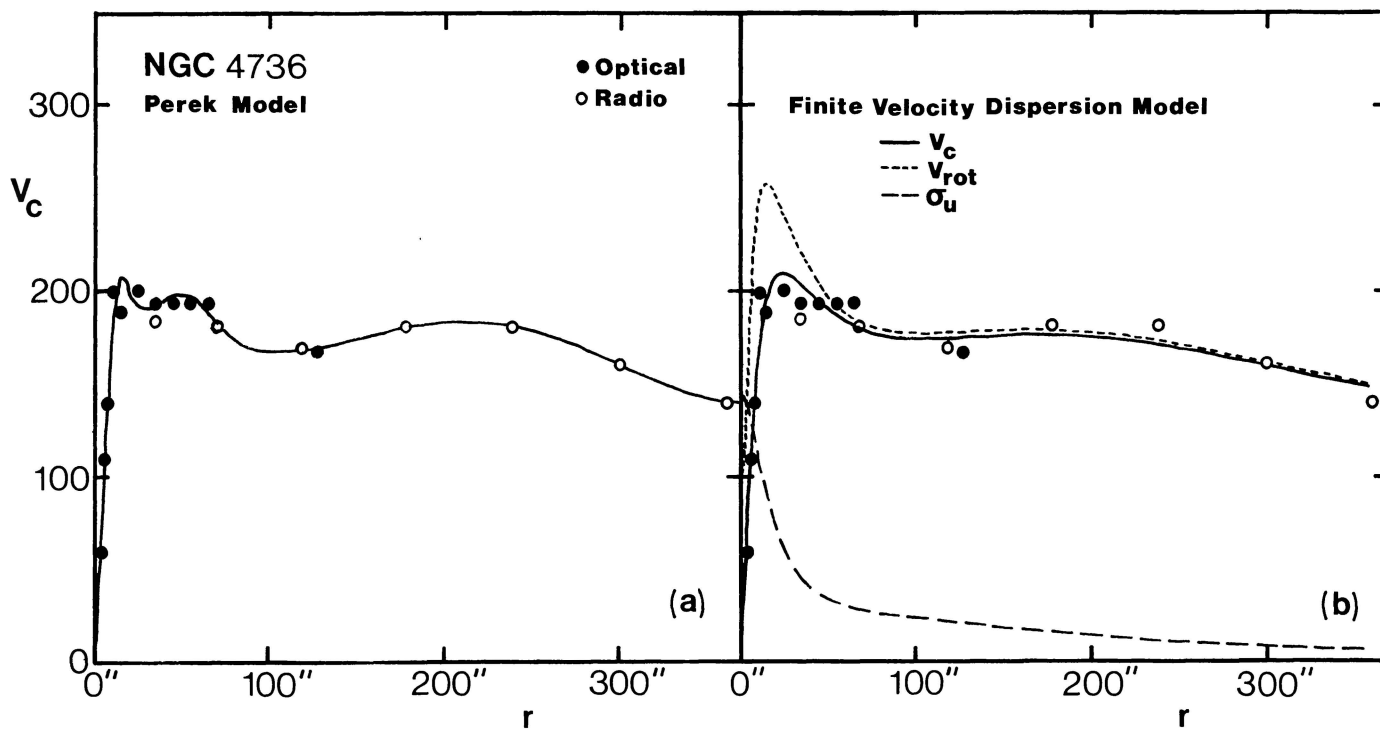


FIG. 6.—Models of the rotation curve of NGC 4736. In (a) is shown a fit based on several inhomogeneous Perek spheroids having a polynomial density distribution of index $n = 2$, while (b) shows a two-component model having finite velocity dispersion in the disk. In this latter model, V_{rot} is the rotation component of the velocity, while σ_u is the radial velocity dispersion. The open circles denote radio observations obtained by Bosma, van der Hulst, and Sullivan (1977), but note that the fits were made using only the optical observations for $r < 100''$, and both the optical and radio observations for $r > 100''$.

TABLE 11
PARAMETERS FOR SINUSOIDAL COMPONENTS MODEL

Parameter	NGC 1512	NGC 3351	NGC 4725
(1) θ_0 (receding half)	261°	195°	25°
(2) i	35°	40°	50°
(3) V_{sys} (km s ⁻¹)	889	779	1192
(4) a_0	79''	74''	141''
(5) θ_0'	126°	96°	40°
(6) q_0	0.79	0.89	0.73
(7) Ω_p (km s ⁻¹ arcsec ⁻¹) ...	-1.8 ± 0.3	2.1 ± 2.2	-1.3 ± 0.1
(8) A (km s ⁻¹)	-66.4 ± 3.9	81.6 ± 6.4	-84.9 ± 3.2
(9) B (km s ⁻¹)	17.5 ± 6.0	0.5 ± 9.5	19.7 ± 4.3
(10) C (km s ⁻¹)	16.3 ± 0.9	-10.2 ± 0.6	26.1 ± 1.0
(11) Ω (km s ⁻¹ arcsec ⁻¹) ...	-2.73	3.27	-2.01
(12) $F_\theta(\text{max})/\langle F_\theta \rangle$	0.07	0.07	0.12
(13) $\langle v_r \rangle$ (km s ⁻¹)	-190	229	-241
(14) r_{CR} ($v = \text{constant}$)	107''	109''	186''
(15) σ (km s ⁻¹)	9.4	12.1	10.7

PARAMETERS.—(1,2) Orientation parameters, chosen to give a resonance parameter of 0.35 (see text); (3) systemic velocity; (4–6) major-axis radius, position angle, and axis ratio of deprojected orbit; (7) pattern speed consistent with inner second harmonic resonance interpretation; (8–10) constants of the radial and tangential velocities (see eq. [8], Paper II); (11) mean circular angular velocity; (12) ratio of maximum tangential force to mean axisymmetric force (see Paper II); (13) mean total tangential velocity; (14) radius of corotation, assuming constant velocity across the ring; (15) standard deviation of fit.

a) Model Fits

i) NGC 1512

The velocity–position angle diagram of the inner ring was derived by isolating velocity points within an elliptical annulus characterized by a major-axis position angle of 51°, an axis ratio of 0.77, and a radius in the range $59'' \leq r \leq 85''$. Only the pure circular rotation and oval bar orbit models are considered in this case. The first model for circular rotation is shown in Figure 7a and is a good fit to the observations. The systemic velocity, position angle of the line of nodes, and circular velocity are identical with those derived from the WWB method. If an asymmetry is actually present in this curve, the data are too sparse to define it unambiguously. The mean error per point is generally less than 10 km s⁻¹, so that the systematic departure in shape from the pure circular rotation model for position angles less than 100° could be significant.

For the oval bar orbit model, a line of nodes in position angle $\theta_0 = 261^\circ$ gives a resonance parameter of 0.35. Figure 8a shows the appearance of the deprojected orbit, which has an axis ratio of 0.79. The model is shown in Figure 8b, and it predicts a slight asymmetry that is not really ruled out by the data. It is as good a fit to the observations as a pure circular rotation model.

The velocity–position angle diagram of the nuclear ring was obtained by isolating all velocity points within an elliptical annulus having a major-axis position angle of 81.5°, axis ratio 0.79, and radius in the range $7'' \leq r \leq 10''$. These parameters are based on a photograph published by Lindblad and Jorsater (1981). In addition to the TAURUS measurements, 12 measurements by Lindblad and Jorsater (1981) were

utilized as well. These are in good agreement with the TAURUS velocities except near position angles 340° and 75°, where differences in resolution may be causing some slight disagreement. The models fitted in this case, pure circular rotation, rotation plus expansion, and rotation plus contraction, are shown in Figures 7b–7d. The fits are nearly identical for each approach, but in order for the line of nodes to agree with that given by the inner ring, the nuclear ring must be expanding at up to 40 km s⁻¹. This conclusion agrees with that of Lindblad and Jorsater (1981).

ii) NGC 3351

The velocity–position angle diagram for the inner ring was obtained by isolating all the velocity points within the elliptical annulus having a major-axis position angle of 10°, axis ratio of 0.86, and radius in the range $56'' \leq r \leq 76''$. The pure rotation model is shown in Figure 9a. Within the scatter it is a reasonable fit to the observations (see also PRFT). For comparison Figure 9b shows the pure circular rotation fit for all points in the disk region of the galaxy in the radius range $86'' \leq r \leq 250''$, i.e., well beyond the ring. Comparison of the derived parameters shows that the line of nodes changes slightly from the inner ring region to the outer disk.

The sinusoidal components oval orbit model is illustrated in Figure 10b, while the face-on geometry of the orbit is illustrated in Figure 10a. For the adopted orientation parameters, the inner ring has only a slight elongation parallel to the bar. In order to have a resonance parameter of ~ 0.35 , the models require the line of nodes to be in position angle 15°. Owing to the aspect, the model looks almost identical with the pure rotation fit, and in fact the lack of a measurable asymmetry would preclude any precise determination of the pattern speed. This is because of the orientation of the ring, whose intrinsic major axis lies nearly in the line of sight. A closed elliptical orbit viewed in such an orientation would, at its projected minor axis, show purely tangential motion, and the velocity–position angle diagram therefore would not show an adequate asymmetry to distinguish the motion from pure rotation.

iii) NGC 4725

The velocity–position angle diagram of the inner ring was derived by isolating all velocity points within an elliptical annulus having major-axis position angle 40°, apparent axis ratio 0.55, and radius in the range $110'' \leq r \leq 150''$. Three models are considered in this case: pure circular rotation, expanding ring, and oval bar orbit.

Figure 11a shows that, in contrast to the case of NGC 1512 and NGC 3351, pure rotation provides a very poor fit to the kinematics of the NGC 4725 ring. The inclination used is based on an average of two sources (see Table 1) and is somewhat uncertain, but its uncertainty is not the reason for the poor quality of the fit. The best-fitting line-of-nodes position angle, 22°, is significantly less than the value, 27°, derived by application of the WWB method for the rotation curve (over a larger radius range). Figure 11b shows that a much better fit is obtained if the ring is allowed to expand as well as rotate. This model places the line of nodes in about the same position angle (37°) as Boroson (1981) derived from

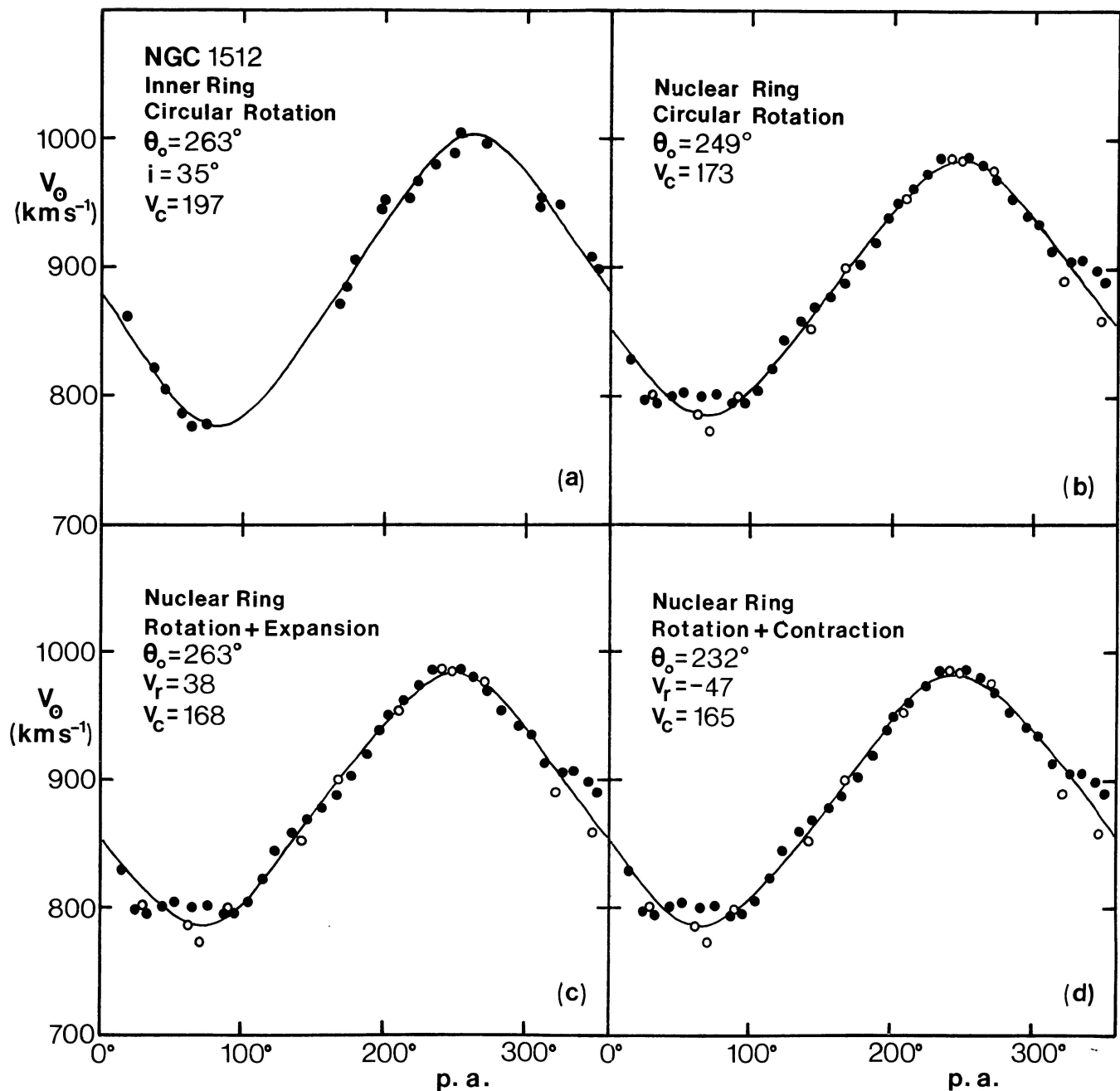


FIG. 7.—Models of the velocity–position angle diagram of the inner and nuclear rings of NGC 1512. The type of fit in each panel is indicated, as is the line-of-nodes position angle appropriate to the fit (an inclination of 35° is used for all the fits). In (b)–(d) the filled circles refer to the TAURUS interferometer data, while the open circles refer to slit spectrum data published by Lindblad and Jorsater (1981). Circular velocities V_c and expansion/contraction velocities V_r are indicated and are denoted similarly in successive figures.

an ellipse fit to a faint outer disk isophote, and as the apparent major axis of the inner ring. The motion is in the sense of an expansion because the near side of the galaxy is on the southeast side of the ring, where the velocity on the minor axis is less than the systemic velocity. The expansion velocity required to explain the observed asymmetry is $51.5 \pm$

7.2 km s^{-1} for the inclination of 57° needed to make the inner ring intrinsically round. This amounts to more than 20% of the mean required circular velocity for the model, $V_c = 218.9 \pm 4.2 \text{ km s}^{-1}$.

These results can be compared with the high-resolution H I observations of Wevers *et al.* (1984, hereafter WADH), who

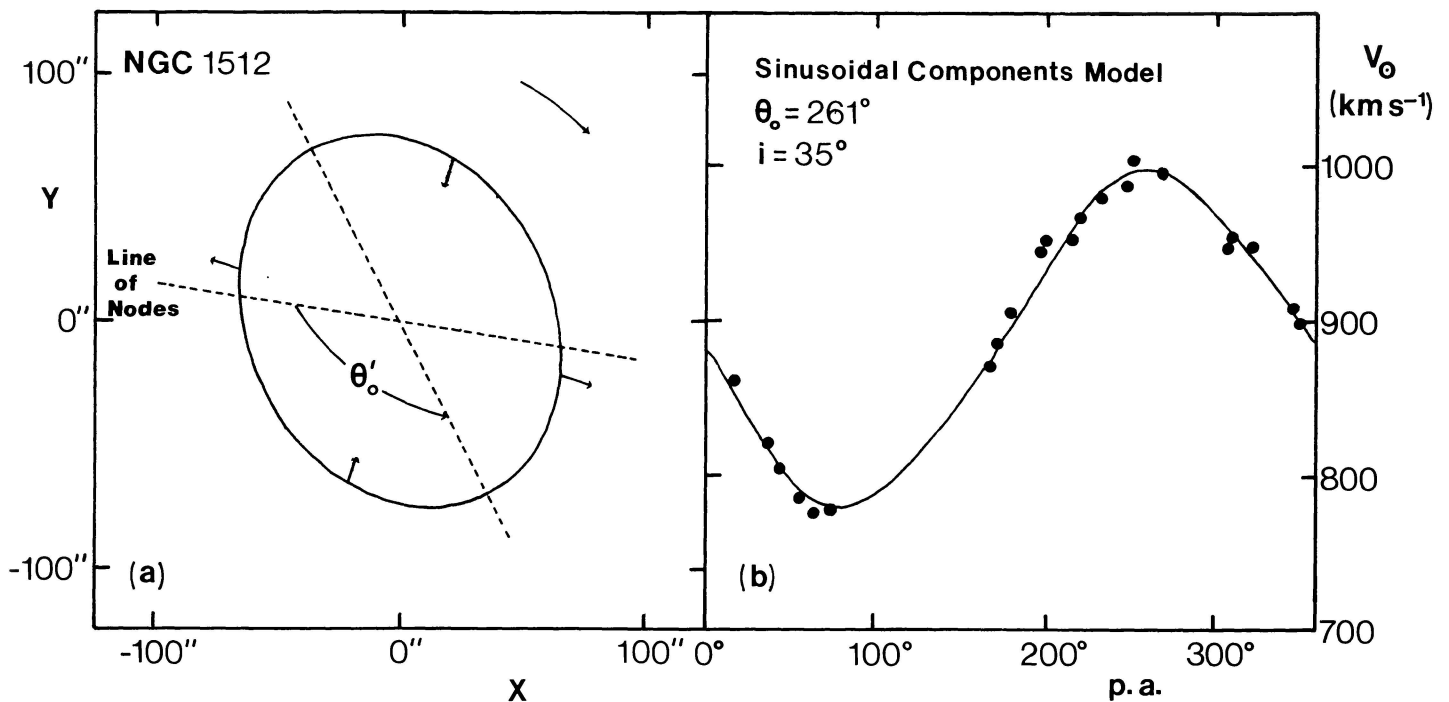


FIG. 8.—(a) Deprojected appearance of the assumed elliptical orbit model for the inner ring of NGC 1512. Arrows indicate directions of the radial velocity vectors and the sense of the rotation. (b) Sinusoidal components oval bar orbit model for the velocity–position angle diagram of the inner ring (see text for details).

studied the kinematics of the NGC 4725–4747 interacting system. These authors found an H I ring of gas nearly coincident in position with the optical inner ring, and measured the velocity–position angle diagram of the feature alone as I have done in the optical. In spite of the differences in resolution, the optical and H I velocities are in excellent agreement on the sense of the asymmetry and the magnitude of the necessary expansion velocity (40 ± 13 versus 52 ± 7 km s^{-1}). However, the H I ring appears to have a major-axis diameter of 2.56 and an axis ratio of 0.64 (versus 2.18 and 0.55, respectively, adopted here for the optical ring), which led WADH to adopt an inclination of 50° to make the ring round. As stated by WADH, emission from part of the innermost arm is probably distorting the H I ellipse somewhat.

While the circular expanding ring model is a promising interpretation of the kinematics of the inner ring of NGC 4725, the presence of an obvious barlike feature nearly crossing the ring major axis suggests a link to the SB(r) inner rings, such as those observed in NGC 1433, NGC 1512, and NGC 3351. At least for NGC 1433, we can determine almost unambiguously that the inner ring is intrinsically oval and aligned along the axis of the bar (Paper II). The average axis ratio of SB inner rings is probably close to 0.8 (Schwarz 1984*a*; Buta 1984; Paper I), and there is evidence that even among nonbarred or weakly barred (SAB) galaxies, there is a significant dispersion in intrinsic shapes. If the ring in NGC 4725 is in fact linked to the presence of the bar, then there is a strong possibility that it is intrinsically oval in shape. In such

a circumstance we must ask whether a stable oval orbit model can provide a tenable description of the kinematics of the ring. To explore this, fits of the sinusoidal components model were made over a grid consisting of inclination values in the range $45^\circ \leq i \leq 55^\circ$ and line-of-nodes position angle $20^\circ \leq \theta_0 \leq 34^\circ$, the pattern speed being varied iteratively until the minimum dispersion about the observed velocity–position angle curve was found. The fits showed first that no sensible orbit model could be fitted if $\theta_0 > 32^\circ$. If $\theta_0 = 38^\circ$, as required by the expanding ring model, then the velocity at the minor axis would be purely tangential, and little asymmetry would be observed in the velocity–position angle diagram. For $\theta_0 \sim 32^\circ$ – 35° , the required pattern speeds are in a sense opposite to the rotation of the galaxy, which is unrealistic. The most reasonable fits require the line of nodes to be in the range $20^\circ \leq \theta_0 \leq 28^\circ$ and yield best-fitting pattern speeds in the range $-1.80 < \Omega_p < -0.8$ $\text{km s}^{-1} \text{arcsec}^{-1}$. Since it is unlikely that θ_0 is less than 20° , these fits all favor the view that the ring lies entirely within CR. The sense of the asymmetry is inconsistent with the reverse motion expected if the ring were entirely outside CR. This result is identical with that found for the inner ring of NGC 1433, but with the disadvantage that we do not have adequate knowledge of the position angle of the line of nodes (independent of the kinematics) to constrain the model. Figure 12*a* shows the deprojected orbit for the orientation parameters which give a resonance parameter of ~ 0.35 , while Figure 12*b* shows the fit to the velocity–position angle diagram. For the adopted inclination of 50° (Table 1), the 2HR[−] resonance identification

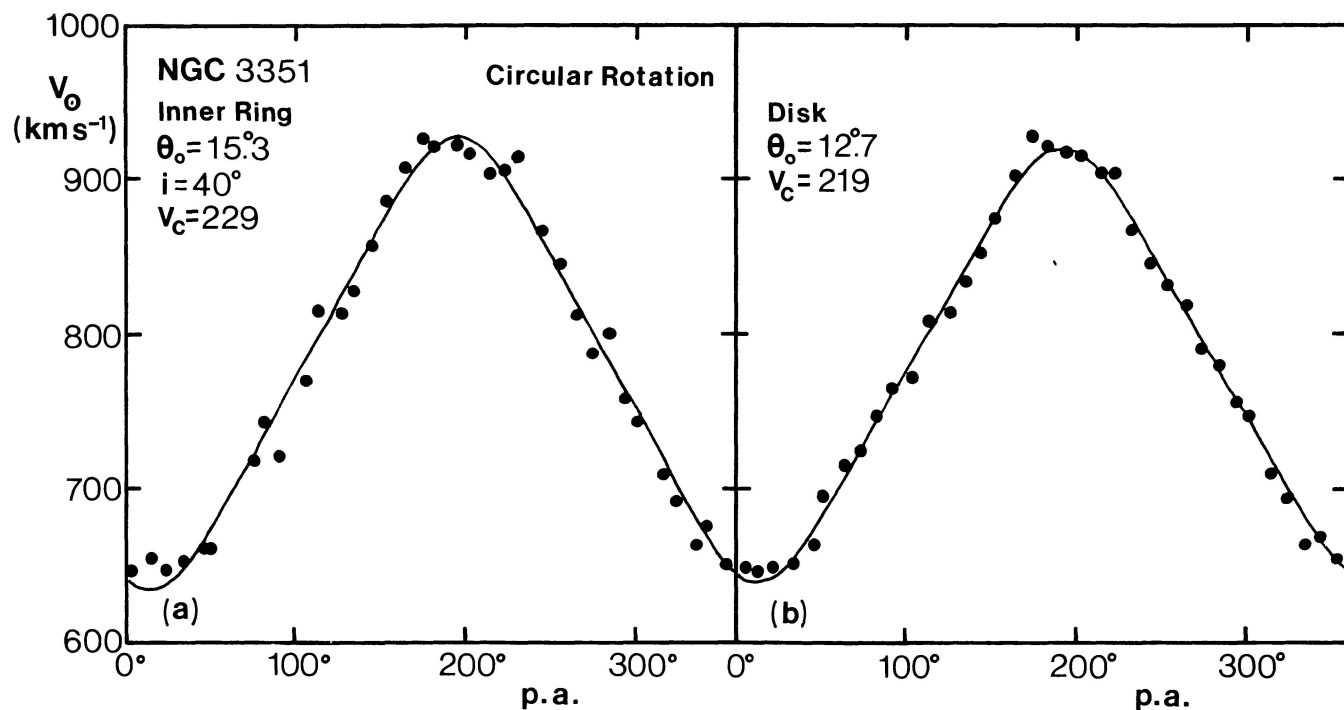


FIG. 9.—Models of the velocity–position angle diagram of the inner ring and outer disk of NGC 3351. Both fits are for pure circular rotation and the indicated inclination.

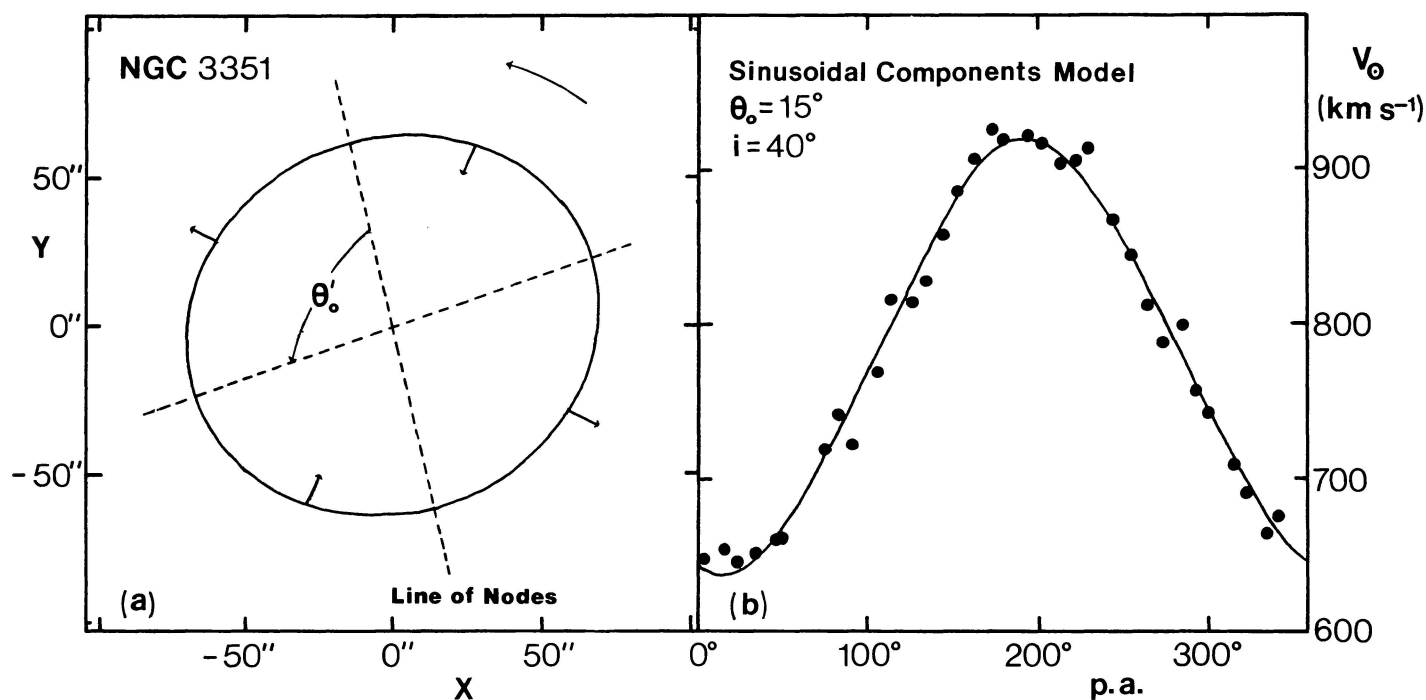


FIG. 10.—(a) Deprojected appearance of the assumed elliptical orbit model for the inner ring of NGC 3351. Arrows indicate directions of the radial velocity vectors and the sense of the rotation. (b) Sinusoidal components oval bar orbit model for the velocity–position angle diagram of the inner ring (see text for details).

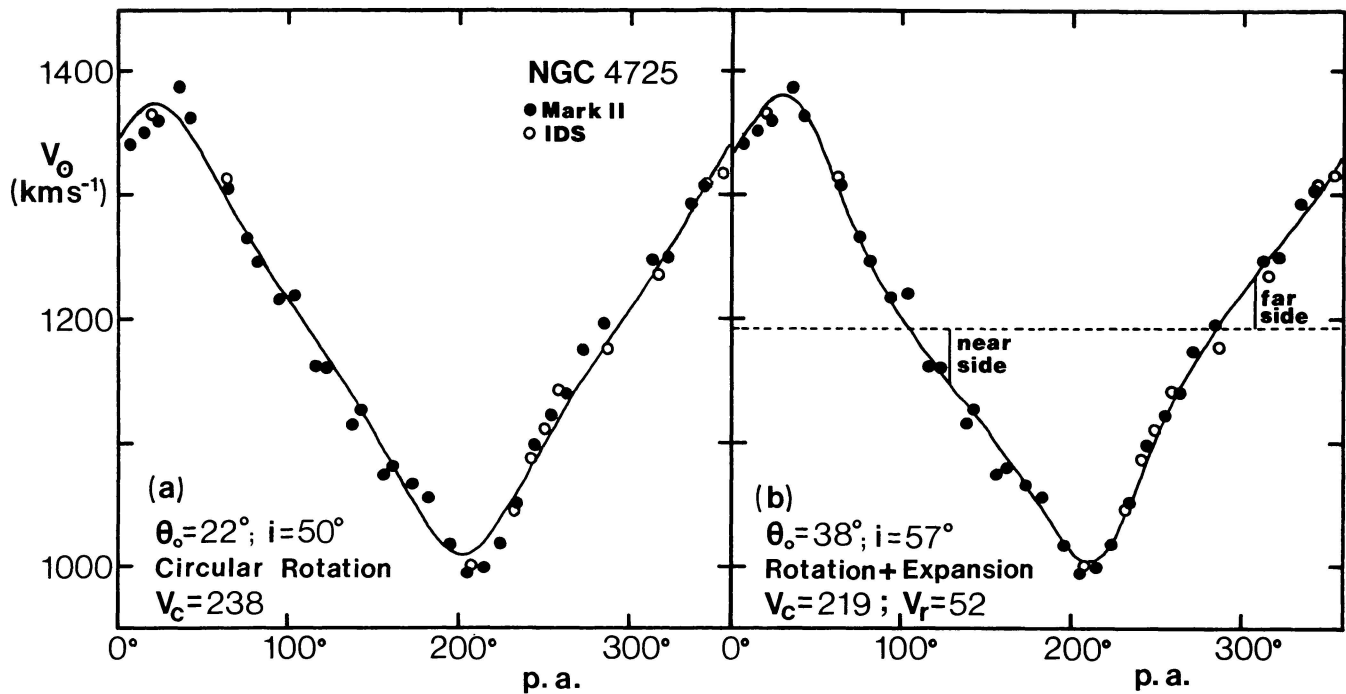


FIG. 11.—Models of the velocity–position angle diagram of the inner ring of NGC 4725. Note the poor quality of the circular rotation fit, and the obvious asymmetry which is well fitted by the expanding ring model. Open circles denote points from IDS observations, while the filled circles denote points from the Mark II interferometer observations. The latter have been adjusted to agree in zero point with the IDS observations (see text).

requires the line of nodes to be in position angle $\theta_0 = 25^\circ$. It is clear that this kind of model can explain the asymmetry in the velocity–position angle diagram nearly as well as the expanding ring model. The noncircular motions required are on the order of 25 km s^{-1} , or about 10% of the mean total tangential velocity (Table 11).

Neither surface photometry nor H I kinematics supports position angles $\theta_0 < 30^\circ$. WADH found that the line of nodes for circular rotation increases from about 30° in the region of the inner ring to 36° in an intermediate region, and then decreases to about 33° in the outer regions. Owing to possible noncircular motions in the inner ring and possible warping in the outer parts due to the interaction with NGC 4747, kinematics in these regions may not provide the most reliable measures of the position angle of the line of nodes. It is clear that unless this parameter and the inclination can be precisely established, a unique model may not be achievable in this case.

iv) NGC 4736

For NGC 4736 the velocity–position angle diagram of the inner ring was obtained by isolating all velocity points in an elliptical annulus having major-axis position angle 125° , an axis ratio of 0.73, and radius in the range $30'' \leq r \leq 65''$. The large radius range was used because the shape of the velocity–position angle curve was found to be insensitive to the radius range as long as the elliptical annulus is centered on the ridgeline of the ring. That is, the unusual effect on the northeast side averages out in this approach. Figure 13 shows

a comparison between the velocity–position angle diagrams derived from the Mark II interferometer data and those derived from the data published by van der Kruit (1976a). This confirms the good agreement between the two sets, and I shall use a mean curve derived from both for the analysis here.

Three simple models were fitted to the radial velocity curve: pure circular rotation, expanding ring, and Lindblad resonance dispersion orbit. I shall use an inclination of 35° (Table 1) for this analysis, although an inclination of 43° would be required to make this ring appear round in the plane of the galaxy (ignoring thickness). In all solutions, however, it was found that the fits were somewhat poorer when 43° was used as opposed to 35° .

The fit for pure circular rotation is shown in Figure 14a. The model is an excellent representation of the data, and it yields a line-of-nodes position angle in good agreement with that derived from the WWB method. There is no sign of an asymmetry in this plot to suggest the presence of significant noncircular motions (e.g., as in NGC 4725), although the points in the range $90^\circ < \text{p.a.} < 130^\circ$ are systematically higher than the model. This is the region where the asymmetry in the rotation curve is found, indicating that it has not quite been averaged out.

If we now assume that the inner ring is circular in its own plane, then the position angle of the line of nodes would have to be about 125° rather than the 116° required for pure circular rotation. This is an average of the major-axis position angle of $122^\circ \pm 3^\circ$ indicated by the appearance of blue-light

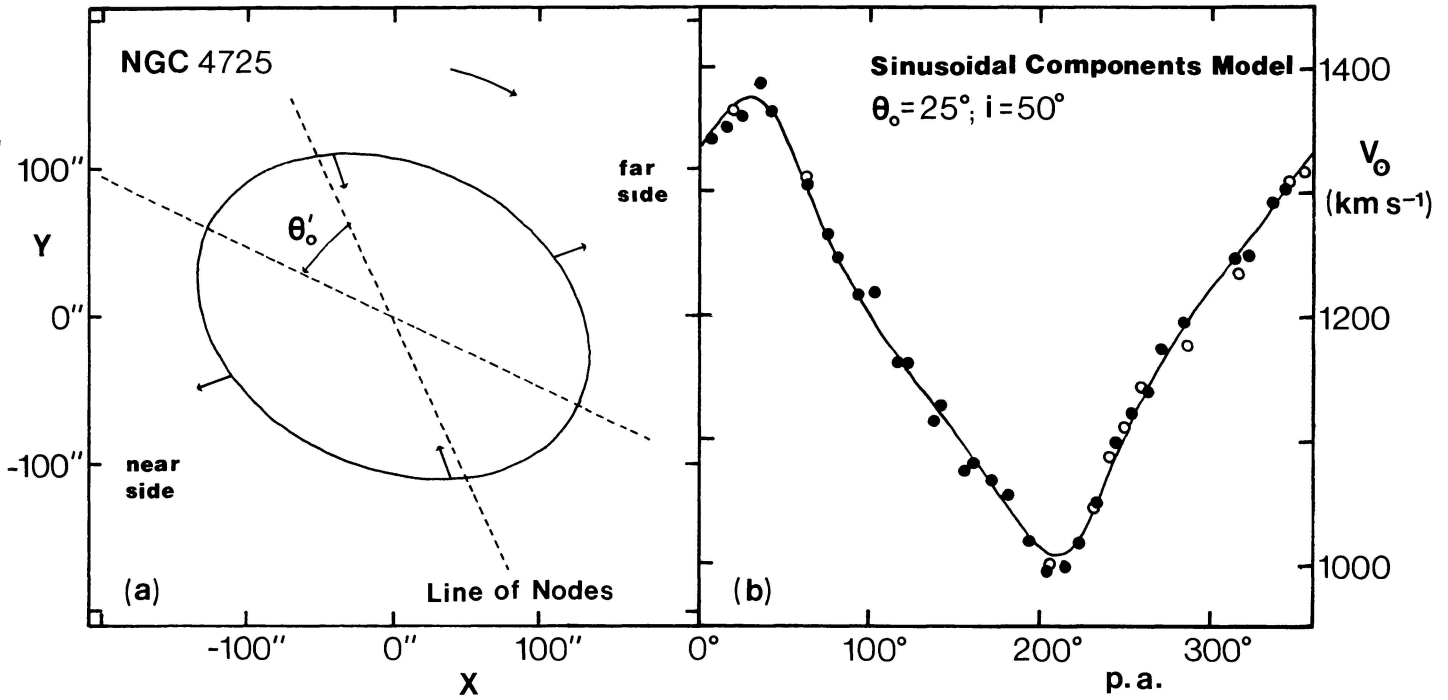


FIG. 12.—(a) Deprojected appearance of the assumed elliptical orbit model for the inner ring of NGC 4725. Arrows indicate directions of the radial velocity vectors and the sense of the rotation. (b) Sinusoidal components oval bar orbit model for the velocity–position angle diagram of the inner ring (see text for details). Note how this model can represent the asymmetry in this diagram as well as does the expanding ring model.

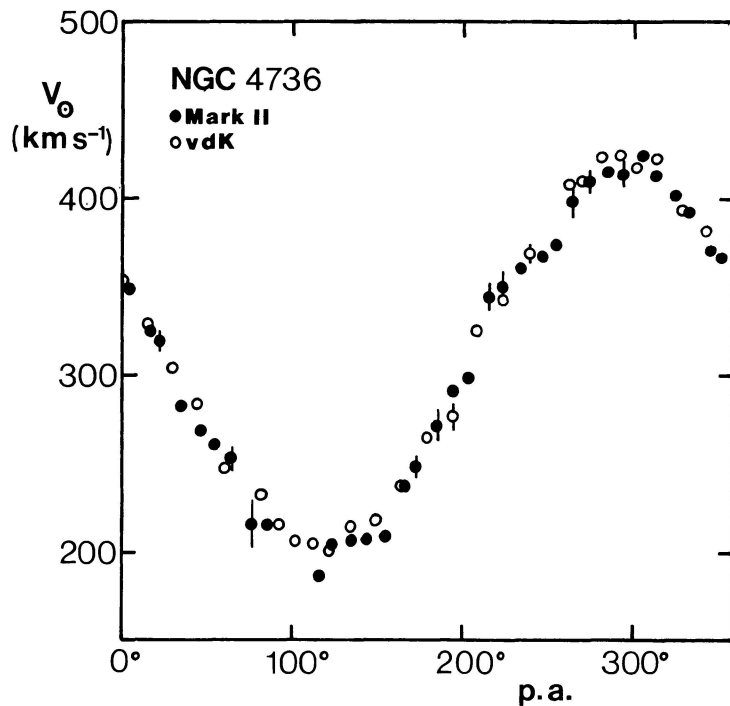


FIG. 13.—Comparison between the velocity–position angle diagrams of the inner ring of NGC 4736 derived from the new Mark II interferometer data and the data of van der Kruit (1976a).

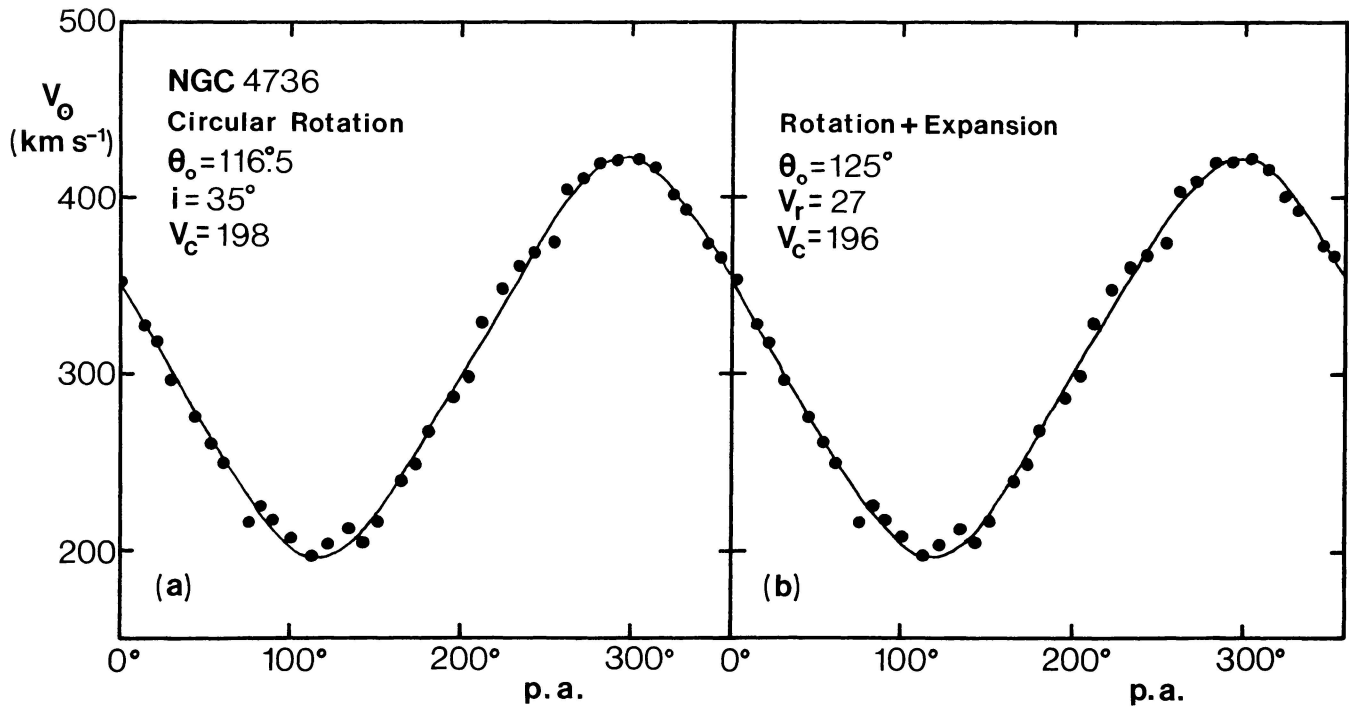


FIG. 14.—Models of the velocity–position angle diagram of the inner ring of NGC 4736. Note how models of pure circular rotation and an expanding, rotating circular ring predict almost indistinguishable fits to the data, but require significantly different values for the position angle of the line of nodes.

isophotes and the position angle, $127^\circ \pm 4^\circ$, of the ridgeline of the H α emission measured by van der Kruit (1976*b*). If 125° is the true line-of-nodes position angle, then to fit the velocity–position angle diagram, one has to add an expansion term in addition to the rotation term. Figure 14*b* shows the resulting expanding ring model for $i = 35^\circ$. The required expansion velocity in this case is $V_r = 27 \pm 2 \text{ km s}^{-1}$, but if $i = 43^\circ$ instead, then $V_r = 22 \pm 2 \text{ km s}^{-1}$. If the line of nodes is not forced to be 125° , but is solved for simultaneously with V_s , V_c , and θ_0 , then the expansion velocity would be $V_r = 35 \pm 22 \text{ km s}^{-1}$ and the line of nodes $127.5^\circ \pm 7^\circ$ for $i = 35^\circ$, or $V_r = 28 \pm 14 \text{ km s}^{-1}$ and $\theta_0 = 127.4^\circ \pm 5.5^\circ$ for $i = 43^\circ$. These results are in excellent agreement with those derived by van der Kruit (1974, 1976*b*). The most disturbing aspect about the expanding ring model is that the inclination is so low that the net effect of the radial term is simply to shift the line of nodes to an apparent value that is displaced $\sim 10^\circ$ from the required true value. The predicted velocity–position angle diagram is seen to be almost indistinguishable from the pure rotation fit.

A dispersion orbit model of the inner ring of NGC 4736 was constructed by assuming that the orbit in projection is defined by the apparent shape and orientation parameters of the ring ($\theta_0 = 125^\circ$, $q_r = 0.73$, and semimajor-axis radius $a = 48''$), and with a known inclination and line of nodes, the parameters of the orbit in the plane of the galaxy were derived. These are the true major-axis position angle, θ'_0 , the guiding-center radius r_0 , the true axis ratio q_0 , and the fractional ellipticity, $\varepsilon = (1 - q_0)/(1 + q_0)$. The model re-

quires a value of the pattern speed, and I have adopted the value $\Omega_p = -1.35 \text{ km s}^{-1} \text{ arcsec}^{-1}$, which places the ring exactly at inner Lindblad resonance (assuming that the velocities on the northeast half of the ring correctly describe the circular motions). The result is not very sensitive to this parameter because the orientation parameters dominate the effects on the observed velocity–position angle diagram. Because there is no reason why the line-of-nodes position angle determined from the pure circular rotation fit should be exactly applicable to this model, that parameter was varied slightly to improve the fit. In all tests the inclination was assumed to be 35° .

The adopted model (Table 12) is shown in Figure 15*b*, while the face-on geometry of the orbit is shown in Figure 15*a*. This latter diagram also shows the directions of the epicyclic velocity vectors. The fit is a good representation of the data, but it requires that the line of nodes be in position angle 119° . The dashed curve in Figure 15*b* shows the velocity–position angle diagram of the guiding-center motions, and it emphasizes how there is little distortion of that motion by the epicyclic velocities, which in this model have amplitudes $V_\theta = 27 \text{ km s}^{-1}$ and $V_r = 19 \text{ km s}^{-1}$. The reason for the small effect of the radial term is that the adopted orientation parameters place the observer's line of sight almost along the true minor axis of the orbit, where the epicyclic motion is predominantly tangential. Because of this and the low inclination, the model predicts no asymmetry in the velocity–position angle diagram but simply shifts the apparent line of nodes.

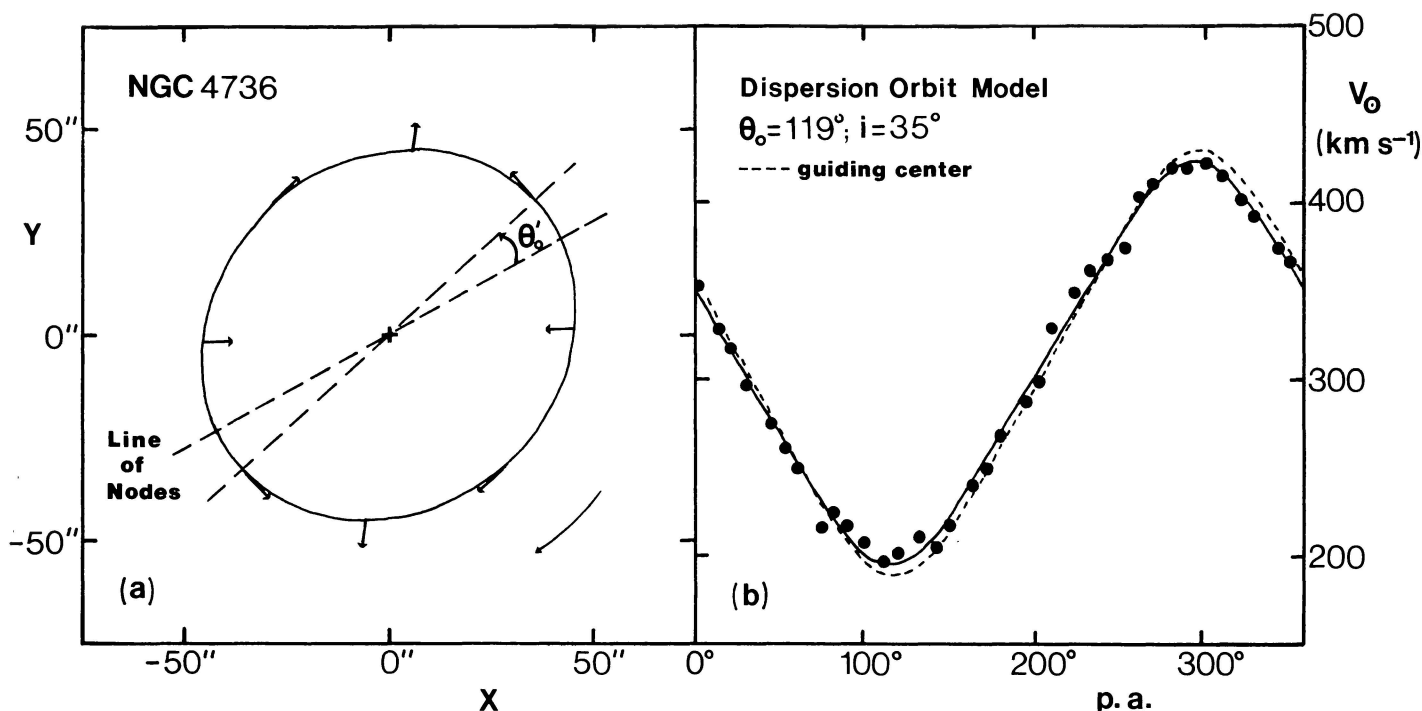


FIG. 15.—Deprojected appearance of the assumed dispersion orbit model for the inner ring of NGC 4736. Arrows indicate directions of the epicyclic radial and tangential velocity vectors and the sense of the rotation. (b) Dispersion orbit model of the velocity-position angle diagram for a best-fitting line of nodes in position angle 119° . The solid curve is the full model, while the dashed curve shows the curve for the guiding-center motions alone, to highlight the small effect of the epicyclic motions.

TABLE 12
DISPERSION ORBIT MODEL FOR NGC 4736

Parameter	Value
(1) θ_0	119°
(2) i	35°
(3) V_{sys} (km s $^{-1}$).....	309
(4) a_0	48''
(5) θ'_0	16°
(6) q_0	0.88
(7) ϵ	0.063
(8) r_0	45''
(9) Δr	2''9
(10) Ω_p (km s $^{-1}$ arcsec $^{-1}$).....	-1.35
(11) Ω (km s $^{-1}$ arcsec $^{-1}$).....	-4.62 ± 0.06
(12) σ (km s $^{-1}$).....	5.99

PARAMETERS.—(1,2) Orientation parameters of galaxy; (3) systemic velocity; (4–6) shape parameters of orbit; (7–9) fractional ellipticity, guiding center radius, and amplitude of the radius variation of the orbit; (10) adopted pattern speed consistent with ILR interpretation; (11) mean circular angular velocity; (12) standard deviation of fit.

To evaluate which of the three models might be most correct, it would be helpful to know the photometric major-axis position angle, since this would be independent of the kinematics. Surface photometry by Boroson (1981) gives $\theta_0(\text{phot}) = 89^\circ$, but this appears to refer to the region just

inside the outer ring, which is probably an oval distortion (Bosma, van der Hulst, and Sullivan 1977). CCD photometry by S. M. Kent (1987, private communication) goes to isophotes 30% larger in radius than the outer ring, and should be more reliable. However, ellipse fits indicate that the orientation and flattening of the isophotes of this galaxy vary continuously with radius and do not settle to any asymptotic value. Over the radius range $350'' < r < 425''$, the photometric major-axis position angle changes from about 106° to 139° , and hence only brackets the kinematic values. Surface photometry therefore does not appear to be helpful in this case, and does not adequately constrain these models.

b) Ring Position Angles

Table 13 gives a useful summary of the measured discrepancy between the kinematic line of nodes for circular rotation and the apparent major-axis position angle of the inner ring for nine ringed galaxies, including NGC 5364 (Buta 1984) and NGC 7723 (Chevalier and Furenlid 1978). This is meant to highlight how the two position angles almost never agree, but are displaced from each other by about 10° on average for six of the objects. The discrepancy is largest for NGC 1433, which is also the best example and which provides the most striking proof that intrinsic elliptical shapes and their accompanying noncircular motions are probably responsible for the misalignments. Although purely circular, rotating rings with uniform expansion or contraction can also produce such discrepancies, the studies presented here and in Papers I–IV provided little evidence for general circular

TABLE 13
COMPARISON OF POSITION ANGLES

Object (NGC) (1)	Type (2)	θ_0 (3)	θ_r (4)	$\Delta\theta$ (5)	θ_{Br} (6)
1433	(R ₁)SB(r,nl)ab	17°	93°	-76°	3°
1512	SB(r)ab	83	51	32	10
3351	SB(r)b	13	10	3	80
4725	SAB(r)ab	27	40	-13	10
4736	(R)SA(r)ab	115	125	-10	...
5364	SA(rs)bc	33	45	-12	...
6300	SB(rs)b	108	123	-15	55
7531	SAB(r)bc	25	14	11	...
7723	SB(rs)c	42	67:	-25:	5:

Col. (2).—Adopted revised type.

Col. (3).—Position angle of line of nodes for circular rotation.

Col. (4).—Position angle of projected major axis of inner ring.

Col. (5).—Difference between these two angles.

Col. (6).—Relative angle between bar and major axis of inner ring in projection.

shapes. It appears that the different lines of evidence—statistics of apparent shapes, kinematics, and comparisons between photometric major axes and ring major axes—all support the fact that rings in general are probably elongated, some quite significantly. This is an important constraint for theories and is one major observation which supports the resonance theory of the rings.

VII. CONCLUSIONS

The kinematic properties of four excellent ringed spiral galaxies have been described. Masses, mass-to-light ratios, and the kinematics of the rings alone have been derived and analyzed. Together with the data on NGC 1433, NGC 6300, and NGC 7531 in Papers II–IV, the following *general* conclusions can be made about ringed spiral systems:

1. H α emission in ringed spirals tends to show its greatest intensity and concentration within the optical rings. The barred spirals NGC 1433, NGC 1512, and NGC 3351 are most similar in having localized concentrations of H II regions in the nucleus and the inner ring, with virtually no emission (detectable within the limits of the interferometer data) between the two rings. Only in NGC 1512 is the distribution of H II in the nucleus of a regular, ringlike form. In NGC 4725, H II regions are also distributed in a ringlike, spiral-like form coinciding with the bright blue inner ring and spiral arm, but there is no bright emission from the nucleus and no nuclear ring. The SA spirals NGC 4736 and NGC 7531 (both of which are probably SAB galaxies to a limited extent) possess smaller, higher surface brightness inner rings than the barred spirals and are also striking in their concentrations of ionized gas. *It is clear that the rings in all of these systems are sharp zones of active star formation.*

2. The rotation curves of ringed galaxies are similar to most other nonringed galaxies in showing a rapid rise to a maximum velocity followed by a more or less constant velocity thereafter. The masses and mass-to-light ratios are normal

for the galaxy types (within the limitations of the mass distribution models), except for NGC 4736, whose unusually high surface brightness in the inner regions leads to a lower than average mass-to-light ratio. In conjunction with detailed luminosity distributions, the rotation curves suggest that ringed galaxies (e.g., NGC 4736 and NGC 7531) also have massive halos, although for one case (NGC 6300) the optical rotation curve data do not extend far enough to allow a clear-cut judgment.

3. The kinematics of rings show considerable variety, but in general the motions are predominantly circular. From a comparison between the major-axis position angle of the inner ring and the line of nodes for circular rotation, we can definitely deduce that on average rings tend to be oval in shape, a fact which also follows from statistical studies of the distributions of apparent axis ratios (Buta 1984; Schwarz 1984*a*; Paper I). Only in NGC 1433 and NGC 4725 can noncircular motions be unambiguously detected in the shape of the velocity–position angle curve. For the others, pure circular rotation models either fit the data best or else give velocities around the ring which are indistinguishable from models of elliptical rings. *The predominant uncertainty in interpreting ring kinematics is the uncertainty in the orientation parameters of the parent galaxies.* Since one cannot necessarily assume that the rings are intrinsically round, and moreover, for strong-barred spirals like NGC 1433, since it may not even be valid to assume that the outer disk is axisymmetric, inclinations are difficult to establish precisely for these galaxies. For NGC 1512 and NGC 4725, interaction with a nearby companion further complicates the derivation of the orientation parameters, and even with reliable surface photometry the situation is no better for NGC 4736 making the interpretation of the kinematics of the inner ring especially ambiguous.

In addition to these general conclusions, we can make the following specific conclusions about individual objects:

1. The inner ring of NGC 1433 is clearly extreme in its intrinsic elongation ($q_r = 0.65 \pm 0.03$). Even given the uncertainties in the orientation parameters of the galaxies, the inner rings of NGC 1512, NGC 3351, and NGC 4725 have intrinsic elongations (for the oval orbit model parameters) of only about 0.80 ± 0.03 , equal to the statistical mean implied by axis ratio distributions (0.8; Paper I).

2. The inner ring of NGC 4725 may provide a strong case for rotation plus *pure* expansion in a ring around a bar. While a model of a perturbed elliptical bar orbit can fit the velocity–position angle diagram of the ring nearly equally precisely, such a model requires the position angle of the line of nodes to be in the range $\theta_0 = 25^\circ \pm 4^\circ$, a range not supported by H I kinematics or orientation estimates from surface photometry. If the circular expanding ring model is in fact correct for NGC 4725, then the origin of the ring is somewhat of a mystery. Uniform expansion could possibly explain why the ring is currently so large intrinsically, but the morphology of the ring suggests that it is most likely a resonance feature associated with a periodic orbit within corotation, and such a feature would not be expected to be circular and purely expanding. If the ring originated in a nuclear explosion that swept all gas from the inner regions, it is currently so large

and expanding with such a high kinetic energy that the explosion energy required would probably be implausibly large. The possibility that the ring may have originated tidally (that is, purely as a result of the interaction with NGC 4747) needs to be explored more carefully. It is presently difficult to make a case for or against a tidal origin.

3. The rotation curve of NGC 4736 is the most unusual of all the cases studied. On one side of the major axis the rotation velocity seems constant, while on the other side there is a significant dip followed by a linear rise only in the ring region. The origin of this asymmetry is a puzzle that remains to be explained, and it clearly complicates the oversimplified models of the kinematics of the ring described here.

4. The inner rings of NGC 1433 and NGC 4725 are significantly miscentered on the optical nuclei. The same is true for NGC 5364 (Buta 1984). While it is conceivable that tidal effects may be responsible for this (both NGC 4725 and NGC 5364 have major companions), the situation is unclear given that NGC 1433 does not appear to be interacting with any other significant object. The cause of ring miscentering is a phenomenon that remains to be explained.

5. The two-ring system of NGC 1512 provides a useful case where we can derive the line of nodes for circular rotation from each ring. The two features are found to require significantly different values for θ_0 , and, given the results from H I kinematics (Hawarden *et al.* 1979), both the data obtained here and the data of Lindblad and Jorsater (1981) indicate that the nuclear ring may be expanding at a significant velocity. Such a feature, which is likely to have its origin in the bar dynamics, is not expected to be purely expanding, since it is probably linked to an inner Lindblad resonance, where, if anything, the systematic effect might be expected to be contraction owing to damping effects (Lynden-Bell and Kalnajs 1972; Schwarz 1979). This makes the origin of the nuclear ring of NGC 1512 also somewhat mysterious, although if the ring is intrinsically elliptical in the plane of NGC 1512, the noncircular motions accompanying this ellipticity may be mimicking pure expansion.

6. Finally, the measurements of the H α to [N II] λ 6583 line intensity ratios given in Table 4 for 10 H II regions in the

inner ring of NGC 4725 allow us to make a judgment of the chemical properties of that ring compared with an H II region in the ring of NGC 3351 observed by McCall, Rybski, and Shields (1985). For the NGC 4725 H II regions, $\langle \log [N \text{ II}] / H\alpha \rangle = -0.50 \pm 0.03$. Lacking knowledge of the H α /H β ratio, I cannot correct this value for reddening, but this correction is expected to be small (Baldwin, Phillips, and Terlevich 1981). According to Figure 14*b* of McCall, Rybski, and Shields (1985), the observed line intensity ratio for the NGC 4725 H II regions is in the high metal abundance zone occupied by many other giant extragalactic H II regions, and hence the NGC 4725 objects may be "normal." However, McCall, Rybski, and Shields (1985) point out that an H II region in the inner ring of NGC 3351 has the highest metal abundance index of any of the ~ 100 H II regions which they observed, prompting them to comment that this object may be "the most important H II region in the sky." Future studies of the chemistry and other properties of individual H II regions and OB associations in rings should provide further insights into the nature of the star formation process occurring in rings.

I would like to thank G. and A. de Vaucouleurs for obtaining the McDonald Observatory Fabry-Perot interferograms which formed the basis for much of the analysis in this paper, and Dr. William D. Pence for programs and helpful assistance in their reduction. Dr. Marshall McCall was of inestimable assistance in helping me to obtain and reduce the IDS observations of NGC 4725, and was directly responsible for the success of those observations. Dr. S. M. Kent very kindly sent me useful information from his new surface photometry of NGC 4736. I owe special thanks to Drs. Keith Taylor and Paul Atherton for their invaluable help with the TAURUS data obtained with the Anglo-Australian Telescope. Finally, I am grateful to Dr. S. M. Simkin for many years ago initiating my interest in NGC 4736, to Drs. A. J. Kalnajs, K. C. Freeman, and M. P. Schwarz for their insights and suggestions concerning barred galaxy and ring dynamics, and to an anonymous referee for many helpful criticisms. This paper is based on my dissertation research.

APPENDIX

AVAILABILITY OF RADIAL VELOCITIES FROM H α FABRY-PEROT INTERFEROMETRY

The Fabry-Perot interferometry on which this paper is based consists of 3138 velocity measurements, of which 619 are for NGC 1512, 1093 are for NGC 3351, 816 are for NGC 4725, and 610 are for NGC 4736. These measurements will be made available to interested persons upon request to the author.

REFERENCES

- Aaronson, M., *et al.* 1982, *Ap. J. Suppl.*, **50**, 241.
 Baldwin, J., Phillips, M., and Terlevich, R. 1981, *Pub. A.S.P.*, **93**, 5.
 Boroson, T. 1981, *Ap. J. Suppl.*, **46**, 177.
 Bosma, A., van der Hulst, J., and Sullivan, W. 1977, *Astr. Ap.*, **57**, 373.
 Bottinelli, L., Gouguenheim, L., Paturel, G., and de Vaucouleurs, G. 1983, *Astr. Ap.*, **118**, 4.
 Buta, R. 1984, *Univ. Texas Pub. Astr.*, No. 23.
 ———. 1986*a*, *Ap. J. Suppl.*, **61**, 609 (Paper I).
 ———. 1986*b*, *Ap. J. Suppl.*, **61**, 631 (Paper II).
 ———. 1987*a*, *Ap. J. Suppl.*, **64**, 1 (Paper III).
 ———. 1987*b*, *Ap. J. Suppl.*, **64**, 383 (Paper IV).
 Chevalier, R., and Furenlid, I. 1978, *Ap. J.*, **225**, 67.
 Chincarini, G., and Walker, M. 1967, *Ap. J.*, **147**, 407.
 Corwin, H., de Vaucouleurs, A., and de Vaucouleurs, G. 1985, *Southern Galaxy Catalogue* (Univ. Texas Monog., No. 4) (SGC).
 Davoust, E., and de Vaucouleurs, G. 1980, *Ap. J.*, **242**, 30.
 de Vaucouleurs, G. 1959, *Handbuch der Physik*, **53**, 275.
 ———. 1963, *Ap. J. Suppl.*, **8**, 31.
 ———. 1979, *Ap. J.*, **227**, 380.
 de Vaucouleurs, G., de Vaucouleurs, A., and Corwin, H. 1976, *Second Reference Catalogue of Bright Galaxies* (Austin: University of Texas Press) (RC2).
 de Vaucouleurs, G., and Pence, W. 1980, *Ap. J.*, **242**, 18.
 Duflot, R. 1962, *C.R. Acad. Sci., Paris*, **255**, 2714.

- Faber, S., and Gallagher, J. 1979, *Ann. Rev. Astr. Ap.*, **17**, 135.
 Garman, L., and Young, J. 1986, *Astr. Ap.*, **154**, 8.
 Hawarden, T., van Woerden, H., Mebold, U., Goss, W., and Peterson, B. 1979, *Astr. Ap.*, **76**, 230.
 Kent, S. M. 1984, *Ap. J. Suppl.*, **56**, 105.
 ———. 1987, *A.J.*, **93**, 816.
 Kormendy, J. 1979, *Ap. J.*, **227**, 714.
 ———. 1982, in *Morphology and Dynamics of Galaxies* (Geneva: Geneva Observatory), p. 115.
 Lindblad, P., and Jorsater, S. 1981, *Astr. Ap.*, **97**, 56.
 Longo, G., and de Vaucouleurs, A. 1983, *A General Catalogue of Photoelectric Magnitudes and Colors in the U, B, V System of 3,578 Galaxies Brighter than the 16th V-Magnitude* (Univ. Texas Monog. Astr., No. 3).
 Lynden-Bell, D., and Kalnajs, A. 1972, *M.N.R.A.S.*, **157**, 1.
 McCall, M., Rybski, P., and Shields, G. 1985, *Ap. J. Suppl.*, **57**, 1.
 Pellet, A., and Simien, F. 1982, *Astr. Ap.*, **106**, 214.
 Pence, W. 1978, *Univ. Texas Pub. Astr.*, No. 14.
 Perek, L. 1962, *Adv. Astr. Ap.*, **1**, 165.
 Peterson, C., and Huntley, J. 1980, *Ap. J.*, **242**, 913.
 Peterson, C., Rubin, V., Ford, W., and Thonnard, N. 1976, *Ap. J.*, **208**, 662 (PRFT).
 Rubin, V., Ford, W., and Peterson, C. 1975, *Ap. J.*, **199**, 39.
 Sandage, A. 1961, *The Hubble Atlas of Galaxies* (Carnegie Inst. Washington Pub., No. 618).
 Sandage, A., and Tammann, G. 1981, *A Revised Shapley-Ames Catalog of Bright Galaxies* (Carnegie Inst. Washington Pub., No. 635) (RSA).
 Schempp, W., and Wolstencroft, R. 1979, in *Photometry, Kinematics, and Dynamics of Galaxies*, ed. D. S. Evans (Austin: Department of Astronomy, University of Texas), p. 453.
 Schommer, R., and Sullivan, W. 1976, *Ap. Letters*, **17**, 191.
 Schwarz, M. 1979, Ph.D. thesis, Australian National University.
 ———. 1984a, *Astr. Ap.*, **133**, 222.
 ———. 1984b, *Proc. Astr. Soc. Australia*, **5**, 458.
 Simien, F., and de Vaucouleurs, G. 1986, *Ap. J.*, **302**, 564.
 Taylor, K., and Atherton, P. 1980, *M.N.R.A.S.*, **191**, 675.
 Tully, R. B. 1974, *Ap. J. Suppl.*, **27**, 415.
 van der Kruit, P. 1974, *Ap. J.*, **188**, 3.
 ———. 1976a, *Astr. Ap. Suppl.*, **25**, 527.
 ———. 1976b, *Astr. Ap.*, **52**, 85.
 Warner, P., Wright, M., and Baldwin, J. 1973, *M.N.R.A.S.*, **163**, 163 (WWB).
 Wevers, B. 1984, Ph.D. thesis, University of Groningen.
 Wevers, B., Appleton, P., Davies, R., and Hart, L. 1984, *Astr. Ap.*, **140**, 125 (WADH).
 Whitmore, B., Kirshner, R., and Schechter, P. 1979, *Ap. J.*, **234**, 68.
 Wilson, R. 1953, *General Catalogue of Stellar Radial Velocities* (Carnegie Inst. Washington Pub., No. 601).

RONALD J. BUTA: Department of Astronomy, University of Texas at Austin, Austin, TX 78712